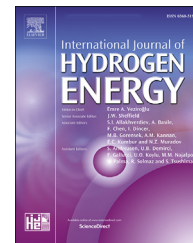




ELSEVIER

Available online at www.sciencedirect.com

ScienceDirect

journal homepage: www.elsevier.com/locate/ijhydene

Hydrogen effects on electrochemically charged additive manufactured by electron beam melting (EBM) and wrought Ti–6Al–4V alloys

Nissim U. Navi^{a,b,1,*}, Jonathan Tenenbaum^a, Eyal Sabatani^b, Giora Kimmel^c, Roey Ben David^d, Brian A. Rosen^a, Zahava Barkay^e, Vladimir Ezersky^f, Eitan Tiferet^{b,g}, Yaron I. Ganor^{b,g}, Noam Eliaz^{a,**}

^a Department of Materials Science and Engineering, Tel-Aviv University (TAU), Ramat Aviv, Tel Aviv 6997801, Israel

^b Nuclear Research Center Negev (NRCN), P.O. Box 9001, Beer Sheva 84190, Israel

^c Department of Materials Engineering, Ben-Gurion University of the Negev, P.O. Box 653, Beer Sheva 841050, Israel

^d Israel Atomic Energy Commission (IAEC), P.O. Box 7061, Tel Aviv 61070, Israel

^e Wolfson Applied Materials Research Center, Tel-Aviv University, Ramat Aviv, Tel Aviv 6997801, Israel

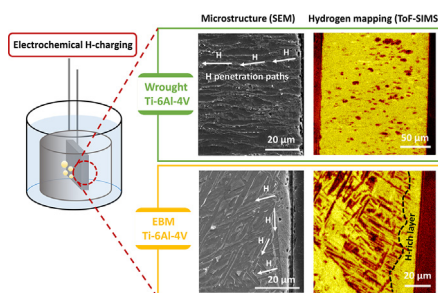
^f Ilse Katz Institute for Nanoscale Science and Technology, Ben-Gurion University of the Negev (BGU), P.O. Box 653, Beer Sheva 84105, Israel

^g AM Center, Rotem Industries Ltd., Mishor Yamin 86800, Israel

HIGHLIGHTS

- Hydrogen behavior in electrochemically charged EBM and wrought Ti–6Al–4V alloys is compared.
- The EBM alloy is more prone to hydrogen-induced cracking at interphase boundaries.
- The surfaces of hydrogenated alloys consist of both solid solutions and hydrides.
- The δ_a and δ_b (fcc) hydrides transform from the α (hcp) phase.
- These hydrides and their lattice constants have not been reported before.

GRAPHICAL ABSTRACT



ARTICLE INFO

Article history:

Received 27 April 2020

ABSTRACT

The hydrogen behavior in electrochemically charged electron beam melting (EBM) and wrought Ti–6Al–4V alloys with a similar β -phase content of ~6 wt% was compared.

* Corresponding author. Department of Materials Science and Engineering, Tel-Aviv University, Ramat Aviv, Tel Aviv 6997801, Israel.

** Corresponding author.

E-mail addresses: nisnavi@gmail.com (N.U. Navi), neliaz@tau.ac.il (N. Eliaz).

¹ Work done during sabbatical leave at Tel-Aviv University.

<https://doi.org/10.1016/j.ijhydene.2020.06.277>

0360-3199/© 2020 Hydrogen Energy Publications LLC. Published by Elsevier Ltd. All rights reserved.

Received in revised form

14 June 2020

Accepted 25 June 2020

Available online 1 August 2020

Keywords:

Additive manufacturing (AM)

Electron beam melting (EBM)

Ti–6Al–4V alloy

Titanium hydride

Hydrogen embrittlement (HE)

Hydrogenation resulted in the formation of microvoids, either adjacent to the surface or along interphases, their coalescence, and emanation of microcracks around them. The microstructure of the EBM alloy displayed a discontinuous arrangement of β -phase particles in the short-transverse direction, a smaller lattice constant of the β -phase, and more α/β interphase boundaries, making the EBM alloy more susceptible to hydrogen embrittlement. The hydrogenated alloys were composed of α_{H} (hcp) and β_{H} (bcc) solid solutions as well as δ_{a} (fcc) and δ_{b} (fcc) hydrides with lattice parameters that have not been reported before. These hydrides were transformed from the primary α -phase. No major microstrain difference was observed between the EBM and wrought alloys, either before or after hydrogenation. Microstrains in the α and β phases increased following hydrogenation; they were larger in the β_{H} and δ_{a} phases compared to the α_{H} and δ_{b} phases. A post-treatment that would increase the size of the β particles is suggested to improve the resistance of EBM Ti–6Al–4V to hydrogen-induced damage.

© 2020 Hydrogen Energy Publications LLC. Published by Elsevier Ltd. All rights reserved.

Introduction

Ti–6Al–4V is widely used in the aerospace, biomedical, and other industries [1–3]. It is the workhorse titanium alloy and has a dual microstructure, which consists of a fine-grained hexagonal close-packed (hcp, α) phase and a distributed body-centered cubic (bcc, β) phase. Elements such as Ti, Al and O stabilize the α -phase, whereas V and H stabilize the β -phase [1,2]. The microstructure and mechanical properties of Ti–6Al–4V are greatly dependent on the thermomechanical processing treatments [4–7]. If the material is cooled too slowly, the β phase becomes more noticeable and lowers the strength and corrosion resistance of the alloy. Hydrogen is sometimes used as a temporary alloying element to improve the manufacturability and final component characteristics of Ti-based alloys, a process known as thermohydrogen processing (THP) [4–6]. Hydrogen alloying results in partial transformation of the low-temperature α -phase into either the high-temperature β -phase or a hydride phase [4]. The properties of $\alpha+\beta$ Ti alloys are determined by the content, size, shape, and morphology of the α -phase and the density of the α/β interphases [8]. Interstitial atoms such as O, N and C increase the strength significantly. The extra-low interstitials (ELI) grade, containing small amounts of O, C, N and H, is commonly used for biomedical applications [2].

Ti and its alloys are susceptible to hydrogen embrittlement (HE) [9], most often by the hydride-formation mechanism [10]. The diffusivity and solubility of hydrogen in the α and β phases are significantly different. The hcp unit cell contains two tetrahedral and one octahedral interstitial sites per metal atom, each with a size of 0.225 or 0.414 metal-atom sphere radius, respectively [11]. In contrast, the bcc unit cell contains six tetrahedral and three octahedral interstitial sites per metal atom, each with a size of 0.291 or 0.155 metal-atom sphere radius [11]. Consequently, both the diffusivity and solubility of hydrogen in β -Ti are higher than in α -Ti [11–18]. Nevertheless, a wide variation is noticed in the diffusivity [17,19] and solubility [14] values for hydrogen in Ti–6Al–4V, which is attributed to dependence on microstructure and β -phase content. When the β -phase content is significant, hydrogen can

favorably diffuse within the β -phase and react with the α -phase at the α/β interphase boundaries.

Hydrogen incorporation in solid solutions of α and β phases results in lattice expansion. This leads to induced strain and to precipitation of hydride phases, three of which are known at room temperature: δ -hydride (face-centered cubic, fcc), ϵ -hydride (tetragonally distorted fcc or face-centered tetragonal, fct, with $c/a \leq 1$), and metastable γ -hydride (fct with $c/a > 1$) [13,15,16,18,20–26].

Machining of titanium is not cost-effective, whereas cast Ti alloys have low fatigue strength and low elongation compared to wrought Ti alloys. Additive manufacturing (AM) allows to produce complex, intricate, geometries and small dimensions with high precision, which is not attainable in casting or milling of Ti alloys [2,8,27]. The microstructure, physical and mechanical properties of AM parts are affected by many variables including the raw powder characteristics, energy density, solidification rate, atmosphere, layer thickness, etc. [18,28]. During manufacturing, the parts are subjected to repeated solid-state and liquid-solid phase transformations, rapid solidification, and directional cooling [29,30]. The combination of these has a profound effect on the microstructure of the deposited material [29,30]. Different AM technologies yield different microstructures and phase compositions of Ti–6Al–4V products, thus resulting in different product properties [18,31–35]. For example, the microstructure of electron beam melting (EBM) Ti–6Al–4V typically consists of a lamellar α -phase (Widmanstätten structure) and a small amount of β -phase within the prior β columnar grains oriented along the build direction, whereas the microstructure of selective laser melting (SLM) Ti–6Al–4V typically consists of columnar β grains and α' martensite due to the fast cooling rate [32,36,37].

Hydrogen may enter an AM material during its processing (e.g., due to moisture absorption in the feedstock powder) [38], post-treatments (e.g., thermal treatment, welding, electroplating, cleaning, acid pickling and etching, or electrochemical machining), or service (e.g., due to corrosion or impressed current cathodic protection). The microstructure of Ti alloys plays an important role in their interaction with hydrogen [18,39]. Exposure of Ti-based alloys to hydrogen

might result in formation of metal hydrides, HE, cracking, and catastrophic failure. It has been shown that the beam current in EBM of Ti–6.5Al–3.5Mo–1.5Zr–0.3Si alloy affects its hydrogen sorption in gas phase due to microstructural changes [40]. While AM of Ti–6Al–4V and the interaction of wrought Ti–6Al–4V alloy with hydrogen have been studied extensively, only few papers have been published on hydrogen interaction with AM Ti–6Al–4V [17,18,26,41,42]. In all of those studies, gaseous hydrogen charging was used.

Pushilina et al. [18] charged EBM Ti–6Al–4V with hydrogen from a gaseous phase at 650 °C to 0.29–0.90 wt% H in the alloy. Hydrogenation to concentration of 0.29 wt% H led to the formation of an intermetallic Ti₃Al phase. As the concentration of hydrogen was increased to 0.58 wt% H, nano-sized crystals of δ -TiH started to precipitate. As the concentration of hydrogen was further increased to 0.90 wt% H, individual Ti₃Al plates transformed into nanocrystals, and the proportion and size of the hydride plates increased. Pushilina et al. [17] also studied the effect of AM variables on the hydrogen sorption behavior of EBM Ti–6Al–4V. Hydrogenation was performed from a gaseous phase at 1 atm and a temperature of either 500 °C or 650 °C up to 0.3 wt% H. A coarser microstructure resulted in a lower average hydrogen sorption rate at 500 °C. The difference of hydrogen sorption kinetics at 650 °C from different samples was insignificant, and a phase transformation $\alpha_{\text{H}} + \beta_{\text{H}} \rightarrow \beta_{\text{H}}$ was observed. Laptev et al. [41] charged EBM Ti–6Al–4V with hydrogen from the gas phase at 1 atm and 650 °C to hydrogen concentrations between 400 and 1000 ppm followed by aging in helium and rapid cooling to room temperature. Hydrogenation to a concentration of 470 ppm led to the formation of 2.2 vol% γ -TiH. A further increase in the concentration of hydrogen to 650 ppm resulted in a slight increase in the content of the hydride phase, and an increase in the content of the β -phase. When the hydrogen content was further increased to 900 ppm, the contents of γ -TiH and β -Ti decreased, while the formation of a δ -TiH was observed. The introduction of hydrogen resulted in an increase in hardness and wear resistance. This was explained in terms of microstructure refinement and formation of secondary phase precipitates. It was concluded that hydrogen not only interacts with existing defects, but it also induces formation of new defects. Silverstein and Eliezer [26] hydrogenated SLM Ti–6Al–4V from a gaseous phase at 0.5 MPa and 500 °C for 10 h, thus forming hydrides and establishing a presumably homogeneous hydrogen content of ~100 wtppm along the bulk sample. The susceptibility to HE significantly depended on the printing direction. Hydrogen desorption appeared in two peaks; the first peak was speculatively ascribed to dislocations or grain boundaries, while the second peak was speculatively ascribed to decomposition of a Ti-hydride phase. Gaddam et al. [42] reported the effect of hydrogen on the mechanical properties of both cast and EBM Ti–6Al–4V that were first hot isostatically pressed (HIP). Hydrogenation was conducted from the gaseous phase for 2 h under a pressure gradually increased to 150 bar. Exposure to hydrogen resulted in a decrease in the yield strength and ultimate tensile strength, with no effect on tensile ductility. The α colony size was reported as being the most important microstructural feature affecting the tensile and low-cycle fatigue (LCF) properties in hydrogen atmosphere.

To date, no study has been reported on either electrochemical hydrogenation of EBM Ti–6Al–4V or the susceptibility of this alloy to hydrogen-induced damage compared to its equivalent wrought alloy. Such a study is of practical importance since the origin of hydrogen entry in electroplating, corrosion, cathodic protection, some other post-treatments, and service environments is electrochemical. Furthermore, electrochemical hydrogenation is quite different than gaseous hydrogenation. In electrochemical hydrogenation, a much higher hydrogen fugacity (of the order of 10⁶ atm, corresponding to a pressure of 10⁴ atm) can be developed at the metal surface, a higher amount of hydrogen can be absorbed in the metal, the distribution of hydrogen in the bulk metal is less uniform (a concentration gradient often exists), surface damage and formation of defects is more pronounced, both trapping in the bulk metal and trapping at the surface are important, and the reproducibility is lower [43,44]. In addition, a thick and adherent layer of hydride may form on the surface of hydride-forming metals, and the amount of hydrogen charged into the sample cannot exceed the terminal solid solubility (TSS) of hydrogen in the alloy in a following homogenization process [45]. In contrast, gaseous hydrogenation, which is typically performed at high temperature, involves dissociation of the H₂ molecules on the metallic surface of the material, followed by the adsorption and diffusion of the hydrogen atoms into the metallic bulk. In this case, the amount of hydrogen charged is not limited to the TSS of hydrogen in the alloy, and the sample can be hydrided completely [45]. Although it can be argued that Sievert's law can be applied to both charging techniques and that once atomic hydrogen has been absorbed in the metal – the HE effects will be similar regardless of the hydrogen source, material test data acquired from electrochemical hydrogenation may not be treated as identical to the data acquired from testing in high-pressure gaseous hydrogen [43,46–50].

The objective of this work is to compare the behavior of electrochemically charged hydrogen in EBM Ti–6Al–4V alloy to that of the wrought Ti–6Al–4V alloy. We show that EBM Ti–6Al–4V is more susceptible to electrochemically charged hydrogen damage compared to its wrought counterpart due to different microstructure. The relations between alloy microstructure and hydrogen behavior are studied in both EBM and wrought Ti–6Al–4V with a similar β -content of ~6 wt%, following electrochemical hydrogenation at room temperature for 1–4 days.

Materials and methods

Sample preparation from the EBM and wrought Ti–6Al–4V alloys

A tray of Ti–6Al–4V samples was manufactured at the AM Center of Rotem Industries Ltd. (Mishor Yamin, Israel) using an Arcam Q20 Plus EBM machine. A standard Grade 5 spherical powder with a size distribution of 45–106 μm , and standard printing parameters of 60 kV accelerating voltage, beam current of 28 mA, speed function 32 (~2400 mm/s base beam speed) and layer thickness of 90 μm were utilized. The process temperature was kept in the range of 750–850 °C. A chamber

pressure of 4×10^{-3} mbar was maintained with a helium leak valve. Rod specimens were orientated in the XY plane of the tray. Fig. S1 (Supplementary file) shows representative as-built samples with two different geometries. Wrought Ti–6Al–4V Grade 23 (ASTM F136) was produced by Dynamet Inc. (Washington, PA, vendor Barmil Petach-Tikva, Israel). Samples with nominal dimensions of $18 \times 18 \times 0.3$ mm³ were cut by electric discharge machining (EDM), mechanically ground and polished on both sides down to 1 μ m (Fig. S2). The sample surface was activated by rinsing the polished samples in a solution of 2.5 N HNO₃ with 20 g/L NaF for 15 s, followed by rinsing in distilled water. This activation solution is a mild version of the well-known Kroll's reagent, commonly used as an etchant to reveal the microstructure of Ti alloys.

Electrochemical hydrogenation

Electrochemical hydrogen charging was done galvanostatically ($j = -25$ mA/cm²) in a two-electrode cell at room temperature (RT) for 1, 2, 3, or 4 days. The alloy sample was the cathode, while a cylindrical Pd90Pt10 (wt%) was the anode. The electrolyte was H₃PO₄:glycerin (1:2 vol). Glycerin-based electrolytes have been used before [51], also to charge Ti-based alloys [23,52]. Since this electrolyte is viscous, the diffusivity of hydrogen molecules in it is quite low (according to the Stokes–Einstein law), and the equilibrium between hydrogen atom adsorption on the metal surface and hydrogen recombination into molecules in solution (the Tafel reaction) is shifted towards the former [51,53]. This electrolyte is also relatively not corrosive [51]. However, since it is hygroscopic, its use is limited to several experiments only [51,53]. The electrolyte was purged with Ar for 30 min prior charging. Purging continued above the electrolyte during charging to prevent oxygen absorption. A fresh electrolyte was prepared for each experiment. Black residues were observed on the surface of the cathode as well as in the electrolyte after each hydrogenation experiment. The nature of these residues is discussed in the Supporting Information file and Fig. S3 therein, along with variables that affected the characteristics of charging.

Material characterization

Chemical composition and density

The chemical composition (all metals, excluding gases) of the non-hydrogenated alloys was determined by glow discharge optical emission spectrometry [54–57] (GDOES, GD-Profilier 2™, Horiba Jobin Yvon S.A.S., Longjumeau, France). This technique allows measurement of depth profiles of constituent elements (including hydrogen) in a solid specimen by detecting atomic excitation into plasma by a non-thermal glow-discharge (sputtering) source. Advantages of this technique include the ability to analyze large specimens with high depth resolution (a few nanometers), quickly, and with no need for ultrahigh vacuum [56]. The analysis was made on a cross-section (see Fig. S4), thus it reflects the bulk composition, and not surface composition. Radio-frequency (RF) power was applied to a flat sample that seals the 2 mm diameter anode. High purity Ar (99.999%) formed as a plasma

gas at a pressure of 850 Pa, and the ions were accelerated by a power of 50 W with a module of 6 V and a phase of 5 V.

The carbon content was measured by CS–800 carbon analyzer (Eltra GmbH, Haan, Germany). The analysis procedure is as follows. After calibration with carbon standards, the sample is weighed in a ceramic crucible, which is then transferred into an induction furnace (2.2 kW power). The sample is melted in a 99.5% pure oxygen atmosphere, converting carbon into a mixture of carbon monoxide and carbon dioxide. The combustion gases are passed through a dust filter and moisture absorber for purification, and analyzed in infrared (IR) cells based on absorption. The analysis time is 70 s while the typical sample weight is between 100 and 500 mg.

The oxygen, nitrogen, and hydrogen concentrations in the non-hydrogenated alloys were measured by an ONH–2000 oxygen/nitrogen/hydrogen analyzer (Eltra GmbH, Haan, Germany) that is based on the inert gas fusion technique. The measurement principle is IR radiation absorption by gases at specific characteristic spectral wavelengths. The analysis procedure is as follows. After calibration with hydrogen, oxygen, and nitrogen standards, the sample is weighed (100–500 mg) while flushing the cell with inert gas. Then, the sample falls into a graphite crucible where it is melted. The furnace power was 8 kW. Carbon monoxide is generated by the reaction of carbon from the graphite crucible and oxygen from the sample. Hydrogen and nitrogen are emitted in their elemental form. The carrier gas (99.995% pure helium) and sample gasses travel through a filter before entering a copper oxide catalyst, which converts carbon monoxide into carbon dioxide. The latter is measured using IR cells to establish the oxygen content. Nitrogen quantity is measured in a thermal conductivity cell. For hydrogen analysis in the thermal conductivity cell, nitrogen carrier gas (99.995%) and the sample gas pass via a Schuetze reagent, instead of the copper oxide catalyst. The typical analysis time is 2 min.

The densities of the non-hydrogenated alloys were measured by the Archimedes method, using deionized (DI) water at room temperature. This is probably the most common technique for determination of the density of EBM and other AM materials and samples [58–63]. Its pros and cons compared to other techniques for measuring the relative density and porosity, such as micro-computed-tomography (μ -CT), gas pycnometry, and image analysis of metallographic cross-sections, are discussed elsewhere [58–60], Appendix B of [63]. In order to represent the actual density of the bulk material, the rough surfaces of the samples were removed prior to measurement (see Fig. S4).

Microstructural analysis by metallography, electron microscopy, and X-ray diffraction (XRD)

The microstructure was characterized using both a light microscope (AXIS, Zeiss, Oberkochen, Germany) and a scanning electron microscope (SEM, Quanta 200 FEG ESEM) combined with an energy-dispersive X-ray spectroscopy (EDS) detector (Oxford X-Max SDD). The conditions for image acquisition were an accelerating voltage of 20 kV and a working distance between 7 and 10.8 mm. Local EDS analysis was carried out at

20 keV electron beam energy at tens micron sample length scales. In some measurements, namely determination of the chemical composition of specific phases or crack zones, EDS analyses were conducted at the micron-scale. Sample preparation for microscopic characterization included mechanical grinding and polishing down to 1 μm , followed by chemical etching in Kroll's reagent (10 mL HF, 30 mL HNO_3 , 50 mL H_2O) [64]. Samples for SEM were coated with a Pd/Au thin layer to enhance microstructural and elemental analysis.

Complementary transmission electron microscopy (TEM) analysis was used to determine the local phase composition. Imaging was carried out using a JEOL JEM-2100 F analytical TEM operating at 200 kV and equipped with Gatan 894 US1000 camera and a JED-2300 T EDS detector. The probe size during the analysis was set to 1 nm. Probe tracking (drift correction) contributed to the high spatial resolution, resulting in high sensitivity analysis at the nanometer scale. JEOL Analytical Station software (v. 3.8.0.21) was used for EDS data analysis. The quantitative analysis was performed by the standardless Cliff-Lorimer method with calculated k-factors. For elements with atomic numbers greater than 12, the k-factors can be determined with an error in the range of 1–4%, while the determination of k-factors for light elements is normally less accurate.

The TEM sample was prepared by Helios NanoLab 460F1 DB focused ion beam (FIB) instrument. The FIB is equipped with high-resolution SEM and a micromanipulator for in situ lift-out technique. It can produce thin (down to 20–30 nm) and uniform lamella thanks to its low ion energy and ion beam control capabilities. Using this technique, a careful extraction of a section from the sample's surface was possible.

XRD at room temperature was used for phase identification, phase content and microstrain analysis of the sample's surface. XRD measurements were performed using a D8 ADVANCE diffractometer with a Bragg-Brentano geometry (Bruker AXS, Madison, WI, USA) and $\text{Cu-K}\alpha$ radiation source ($\lambda = 1.5418 \text{ \AA}$). A linear position sensitive device (PSD) detector (LYNXEYE XE-T) was used, with an opening of 2.94° . Data points were acquired at increments of 0.02° and acquisition time of 0.25 s. The scan was within the range of $2\theta = 10\text{--}100^\circ$, but information was fit from 30° since no useful information was at lower angles. The lattice parameters were fit using TOPAS software, ver. 5 (Bruker AXS, Madison, WI, USA), fitting for the zero-error, lattice parameters, microstrain and phase composition. NIST Si 640e and LaB_6 660c standard reference materials were used to calibrate for peak position and peak shape, respectively. Peaks were fit using a TCHZ function type where U, W, V and the asymmetry parameters were measured using LaB_6 660c and fixed to account for instrumental contributions to peak shape. As a Round Robin procedure, in order to validate the XRD refinement results obtained as described above, non-hydrogenated samples were also analyzed by the X-ray powder diffraction (XRPD) method in theta/theta Bragg-Brentano (reflection) geometry. To this aim, a Panalytical Empyrean powder diffractometer (K_α radiation, $\lambda = 1.5418 \text{ \AA}$) equipped with an X'Celerator linear detector (silicon-based position sensitive line detector) and operated at $V = 40 \text{ kV}$,

$I = 30 \text{ mA}$, was used. The XRD patterns were analyzed for phase fractions using FULLPROF software [65].

Hydrogen mapping and desorption analyses using time-of-flight secondary ion mass spectrometry (ToF-SIMS) and temperature programmed desorption mass spectrometry (TPD-MS)

ToF-SIMS [66–71] was used to map total hydrogen, titanium hydrides, carbon and oxygen and to correlate their local intensity to microstructural features in the Ti alloys, as well as to draw local hydrogen line scan profiles, determine the average normalized intensities of both overall hydrogen and titanium hydrides, and obtain the mass spectra. A Physical Electronics TRIFT II system was used to this aim. A 15 keV, 600 pA Ga^+ ion beam was used to acquire mass spectra, while 25 keV, 60 pA Ga^+ ion beam was used for imaging. The negative secondary ions H^- , TiH^- , and Ti^- were used for imaging of the sample's fine-polished section. Before analysis, a 2 keV, 150 nA Cs^+ ion beam was used for sputtering of the damaged surface layer due to mechanical polishing. Sample mounting was done with glue. Consequently, optimal vacuum conditions could not be reached. A notable outgassing kept the vacuum at about $1\text{--}2 \times 10^{-9}$ Torr, thus causing a high background level of hydrogen in the analytical chamber. Ion images were collected from the fresh surface after Cs^+ sputtering. Cs^+ sputtering is common for hydrogen depth profiling because H^- is more sensitive than H^+ , and Cs^+ sputtering can enhance yields of negative ions [69,71]. In order to reduce the effect of residual hydrogen in the chamber (the glue being a notable source), ion images were collected in a dual beam mode [69], i.e. like in depth profiling. A short stage of image collection with Ga^+ analytical gun was followed by a short sputter stage with Cs^+ sputter gun. Large hydrogen intensity variations due to different crystallographic phases were evident. Therefore, comparison between the samples was done using the average hydrogen content in the analysis area. The accuracy of the SIMS analysis was several percent. In the absence of calibration standards, absolute concentrations cannot be reported herein.

The hydrogen desorption profile and the total amount of hydrogen desorbed from the hydrogenated alloys were determined by TPD-MS. A detailed description of the home-made TPD-MS system utilized in the present study can be found in Ref. [72]. The system was calibrated for quantitative hydrogen analysis using a standard of TiH_2 powder (Sigma Aldrich, 98% purity), which contains a stoichiometric amount of hydrogen (4 wt%) [73]. For each TPD measurement, a typical sample mass of $\sim 30 \text{ mg}$ was utilized (loaded inside a quartz crucible), and three to four duplicates were measured for each type of specimen. The samples were heated from room temperature to 950°C at constant heating rates between 10 and $20^\circ\text{C}/\text{min}$ under a 50 mL/min flow of high-purity He. Procedures for data analysis of TPD results (also known as thermal desorption spectroscopy, TDS) are explained in Refs. [44,51], while examples for the use of our homemade system [72,74] as well as the use of TPD/TDS method in the study of hydrogenated Ti-based alloys [21,23,25,26,75,76] can be found elsewhere.

Table 1 – Chemical composition (wt%) of the non-hydrogenated EBM and wrought Ti–6Al–4V alloys.

Element	Wrought	AM
Ti	90.485 ± 0.006	90.649 ± 0.006
Al	5.558 ± 0.003	5.458 ± 0.003
V	3.674 ± 0.005	3.589 ± 0.005
Fe	0.232 ± 0.001	0.234 ± 0.001
Mo	0.049 ± 0.000	0.047 ± 0.000
Cr	0.022 ± 0.000	0.014 ± 0.000
Mn	0.009 ± 0.000	0.009 ± 0.000
C	0.0069 ± 0.0007	0.0145 ± 0.0014
O	0.1296 ± 0.0064	0.2554 ± 0.0128
H	0.0200 ± 0.0012	0.0120 ± 0.0008
N	0.0086 ± 0.0008	0.0676 ± 0.0060

Results

Chemical composition and density

The chemical composition of the non-hydrogenated alloys is given in Table 1. The chemical composition of the EBM alloy matched the specification of ASTM F2924 [77], except a minor deviation in the Al content. The chemical composition of the wrought alloy was in agreement with ASTM F136 [78]. The average density of the EBM and wrought alloys were 4.421 ± 0.001 and 4.424 ± 0.001 g/cm³, respectively.

Hydrogen-induced cracking and stability of samples over storage time

While handling the hydrogenated samples it became clear that both the wrought and the EBM alloys were embrittled by hydrogen. After four-day hydrogenation, brittle cracking was evident in both cases due to hand fracturing (Fig. S5).

In the first stage of this study, the possible effect of sample storage time on the concentration of hydrogen and the phase content in hydrogenated samples was evaluated. It was concluded that the results should not be affected by the storage time because: (1) the diffusivity of hydrogen in Ti–6Al–4V is not high at room temperature [17,19]; (2) previously reported TPD measurements showed no evidence of hydrogen desorption from Ti–6Al–4V at room temperature [26]; (3) thermal desorption from samples stored in liquid nitrogen was not evident at room temperature, but started only at 420 °C; (4) the XRD pattern of a sample hydrogenated for one day did not change as a result of storage of up to 126 days (twice longer than the maximal aging time from hydrogenation to TPD measurements in this study).

Microstructure and local chemical composition

Fig. 1a and b shows optical micrographs of non-hydrogenated wrought and EBM alloys, respectively. The primary α and transformed β phases appear bright and dark, respectively [16,34,79]. The microstructure of the wrought alloy (Fig. 1a) consisted of large elongated grains of α -phase and a lamellar α/β structure in between. It should be noted that the distribution of the α -phase and the lamellar structure was not

uniform in the bulk wrought alloy; some regions were richer in the large α -phase while others were richer in the finer lamellar structure. The microstructure of the as-built EBM alloy (Fig. 1b) was made up of a fine acicular (thickness of a few micrometers or less) α -phase, the boundaries of which were surrounded by β -phase. Within prior β grains, a transformed $\alpha+\beta$ microstructure with both colony and Widmanstätten morphology with different orientations were observed. The β -phase was not continuous across the sample. This microstructure results from rapid solidification that is associated with the EBM process and the thermal gradient in the z-direction and is manifested, among others, by columnar growth of the prior β grains [17,32,35,37]. No cracks or significant voids were observed in both materials. Although some articles have reported grain size measurements in wrought [80] and AM [81] Ti–6Al–4V alloys, the accuracy of the measurements are debatable. Therefore, in spite of our attempt to make such measurements both manually (referring to ASTM standards E1181, E1382, and E112) and automatically (using ImageJ image analysis software), values are not reported herein.

After one-day hydrogenation, new microvoids became apparent, both adjacent to the surface and in the bulk of the wrought alloy. Some coarsening and reorientation of the bright phase/s was evident in the microstructure of the EBM alloy, compared to the non-hydrogenated EBM alloy, along with the development of a dark boundary along the long, continuous bright (lath) phase. After two-day hydrogenation, the number of voids increased in the wrought alloy, and cracks were initiated in the EBM alloy. After three-day hydrogenation, the number of voids did not seem to increase in the wrought material, no cracks were observed, and reduction in the bright region (i.e., either α or α_H phase) was observed (Fig. 1c). A brittle crack was observed in the EBM sample (Fig. 1d) after three-day hydrogenation. The path of the crack is clearly along the boundary between the long, continuous white (lath) phase and its surrounding. The high density of α/β interphase interfaces in the EBM alloy could favor local hydride nucleation and growth [82]. Microvoid coalescence was also evident along this interphase boundary. In general, the level of porosity/microvoids in the EBM alloy was higher than in the wrought alloy.

After four-day hydrogenation, the amount of voids did not seem to further increase in the wrought material (Fig. 1e), but further reduction in the bright region was observed. The large bright grains of the wrought material were oriented in parallel to the short transverse direction of the sample. The microvoids formed preferentially at the boundaries between the α/α_H and β/β_H phases, but no cracking along interphase boundaries was evident in the wrought material. Neither hydrogen-induced formation of α'' martensite plates nor increase in the total $\beta+\beta_H$ content compared to the non-hydrogenated alloy was evident. No distinct difference was evident in the microstructure of the EBM alloy after four-day hydrogenation (Fig. 1f) compared to three-day hydrogenation, except some decrease in the $\alpha+\alpha_H$ content.

Fig. 2a,b and Fig. 2c show SEM images of the cross-sections of non-hydrogenated wrought and EBM alloys, respectively. The microstructure of the non-hydrogenated wrought alloy (Fig. 2a, b) consisted of a matrix of an equiaxed primary α -phase, intergranular β -phase (light-gray), and partially

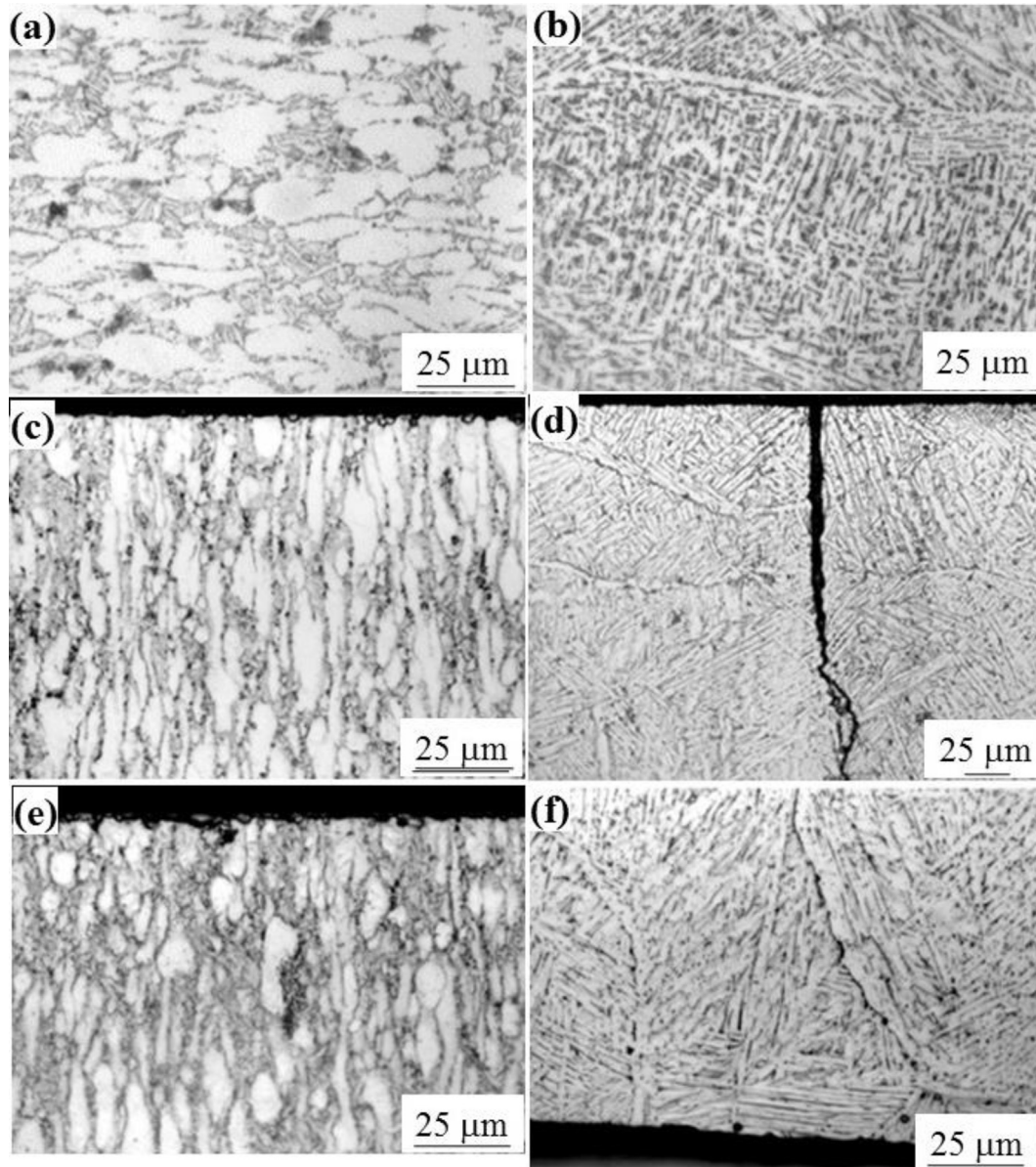


Fig. 1 – Light micrographs revealing the microstructure in metallographic cross-sections after chemical etching in Kroll's reagent. Non-hydrogenated wrought (a) and EBM (b) alloys, wrought and EBM alloys after three (c,d) and four (e,f) days of hydrogenation.

lamellar packets [24,82,83]. The microstructure of the non-hydrogenated EBM alloy (Fig. 2c) consisted of α laths with different sizes and orientations, arranged in a Widmanstätten structure inside the prior β grains, along with β bars embedded in the continuous α -phase [17,18,32]. More pores were distributed in the microstructure of the non-hydrogenated EBM alloy compared to the wrought alloy, which may be expected for a powder bed fusion (PBF) EBM process. Image analysis of the SEM images roughly estimated β -phase contents of 6.1 and 4.8 vol% in the wrought and EBM alloys, respectively. However, more accurate values were obtained from XRD, as will be shown below.

After one-day hydrogenation, some hydrogen-related microvoids appeared in the wrought alloy, mainly adjacent

to the surface (Fig. 2d). After four-day hydrogenation, the number of microvoids increased, in particular in the bulk alloy (Fig. 2e). These voids apparently nucleated and grew around the $\alpha/\alpha_H/\beta_H$ interphase (Fig. 2f). Fig. 2e also demonstrates the continuous pathways for hydrogen diffusion in the short transverse direction in the wrought sample. Higher magnification revealed four different morphologies, which may be related to four different phases (Fig. 2g). The morphology marked #1 in Fig. 2g was not observed in the non-hydrogenated wrought alloy.

After one-day hydrogenation, some hydrogen-related microvoids appeared in the EBM alloy, mainly adjacent to the surface. In addition, a bright reaction zone with a distinct morphology of its own formed near the surface (Fig. 2h). Based

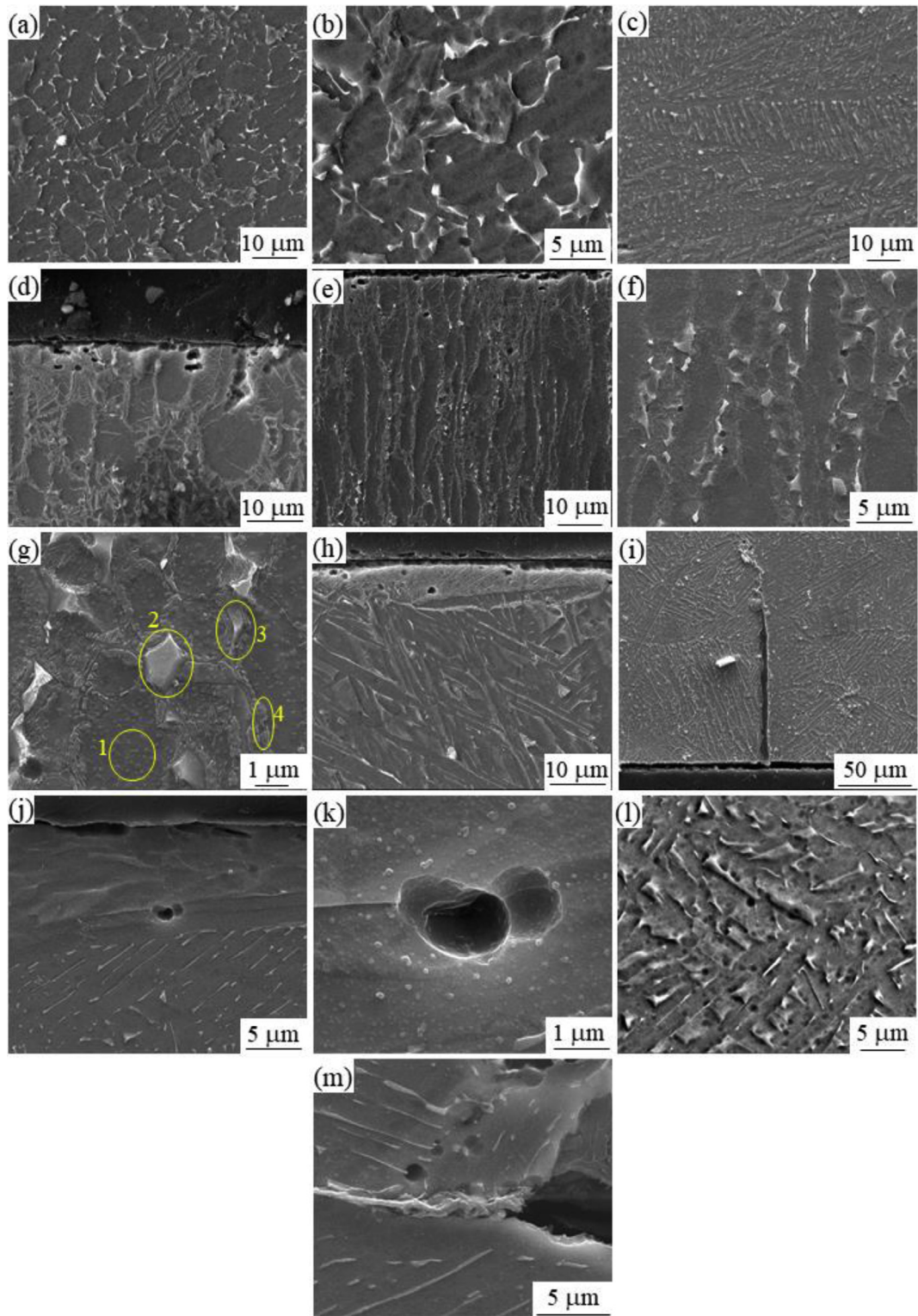


Fig. 2 – SEM micrographs revealing the microstructure in metallographic cross-sections. Non-hydrogenated wrought (a,b) and EBM (c) alloys, wrought alloy after one (d) and four (e–g) days of hydrogenation, EBM alloy after one (h), three (i) and four (j–m) days of hydrogenation. All images are secondary electrons (SE) images, except (l) which is a backscattered electrons (BSE) image. The local chemical composition of the four regions marked in (g) is given in [Table 2](#).

on XRD results (see below), this reaction zone may be related to the formation of titanium hydride, although SIMS mapping did not identify it. After two-day hydrogenation, no further change in the microstructure of the bulk EBM alloy was evident. As described above, a crack was observed in the EBM sample hydrogenated for three days (Fig. 1d). SEM observation (Fig. 2i) revealed that this crack was actually filled by a solid matter. Fig. 2i also demonstrates the non-continuous β -phase pathway for hydrogen diffusion in the short-transverse direction in the EBM sample.

After four-day hydrogenation, the width of the reaction zone adjacent to the surface was essentially unchanged, and microcracks emanating around coalescing microvoids were apparent (Fig. 2j,k). Many more microvoids appeared in the bulk alloy, mainly at α/α_H and β/β_H interphases (Fig. 2l). In several locations, a bright phase with a distinct morphology seemed to fill cavities (Fig. 2m). The location and morphology of this phase are similar to those recently observed by in situ electrochemical hydrogen permeation experiments in a SEM coupled with an electron backscattered diffraction (EBSD) [82]. In that study, this phase was shown to be a titanium hydride in a wrought Ti–6Al–4V alloy.

Table 2 summarizes local EDS data acquired on metallurgical cross-sections of non-hydrogenated wrought and EBM alloys as well as the counterpart materials hydrogenated for four days. For the wrought alloy charged for four days, a comparison is also made between the local composition within zones with four different morphologies in Fig. 2g. For the EBM alloy charged for four days, the composition range in parenthesis represents six different morphologies observed in the microstructure of this alloy. Neither Pd or Pt from the anode nor P from the electrolyte was detected by EDS (the samples for this analysis were not coated with Pd/Au thin layer). The crack in Fig. 2i was found to be filled with a solid material consisting of C, Ti, O, Al, and Cl, the origin of which is likely the mounting resin material. Hydrogenation seemed to decrease the concentration of Ti and increase the concentration of V. Similar trends, along with decrease in the concentration of Al, were reported in Ref. [16] for the α -phase; they were related to α -to- β phase transformation.

XRD phase and microstrain analysis

XRD patterns of non-hydrogenated and hydrogenated EBM samples are shown in Fig. 3. The non-hydrogenated alloy contains two phases: a major α -phase and a minor β -phase with a (101) and (110) texture, respectively. In contrast, the

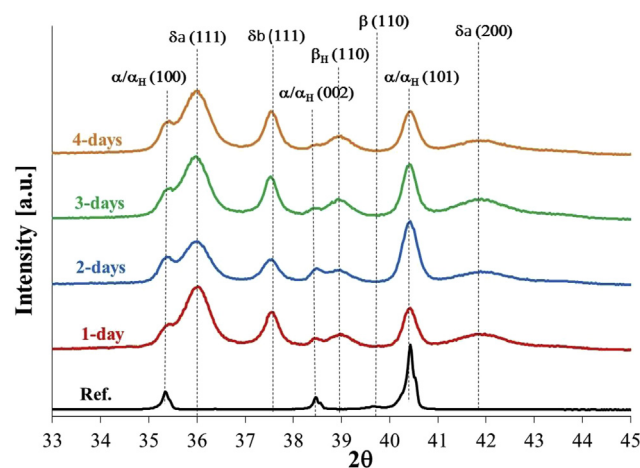


Fig. 3 – XRD patterns of non-hydrogenated and hydrogenated EBM Ti–6Al–4V.

hydrogenated samples contain two designated phases: (1) hcp phase with peak positions similar to the original α -phase of the non-hydrogenated sample. Since peak positions of this phase did not change following hydrogenation, it seems that the majority of this phase is not a solid solution of hydrogen in α -phase (designated herein as α_H). However, since we cannot distinguish between the contents of α and α_H , a reference is made herein to α/α_H or $\alpha+\alpha_H$; (2) β_H -phase (bcc) with peaks shifted to lower reflection angles compared to the original non-hydrogenated β -phase, indicating an increase in the unit cell size of the β -phase due to hydrogenation.

Other peaks in the diffractogram (at $2\theta = 37.6, 43.5$, and 80.3 deg) do not match well other reported phases in the International Center for Diffraction Data (ICDD), such as δ -TiH₂, δ -TiH_x, and γ -TiH. Crystallographic information taken from Refs. [84] was used to manually construct a file for the metastable γ -TiH tetragonal phase. Upon trying to fit this tetragonal phase to our data, many peaks were missing, and it did not fit. The peak at $2\theta = 37.6$ deg can neither be related to $2\theta \approx 36.8$ deg designated in Ref. [85] as γ -TiH nor to the strongest reflection of γ -TiH in ICDD file no. 00-040-1244 ($2\theta = 36.02509$ deg). ICDD file no. 03-065-0139 (γ -TiH) does not match well either, so is ICDD no. 00-059-0236 (TiH_{0.74}).

The undesignated peaks were resolved by matching the peaks to two different phases with an fcc structure (δ -TiH₂-like and δ -TiH_x-like structures), which are attributed to hydride phases and referred hereafter as δ_a and δ_b , both with

Table 2 – Local (EDS) chemical composition (wt%) in non-hydrogenated and four-day hydrogenated EBM and wrought Ti–6Al–4V alloys.

Sample	Ti	Al	V
Wrought, reference	90.61	5.82	3.57
EBM, reference	90.83	5.68	3.49
Wrought, 4-d	89.93	5.93	4.14
Wrought, 4-d, morphology 1 in Fig. 2g	90.80	5.94	3.26
Wrought, 4-d, morphology 2 in Fig. 2g	88.17	5.10	6.73
Wrought, 4-d, morphology 3 in Fig. 2g	89.01	5.70	5.29
Wrought, 4-d, morphology 4 in Fig. 2g	89.99	5.47	4.54
EBM, 4-d	90.51 (86.11–90.61)	5.69 (5.48–6.12)	3.80 (3.21–8.39)

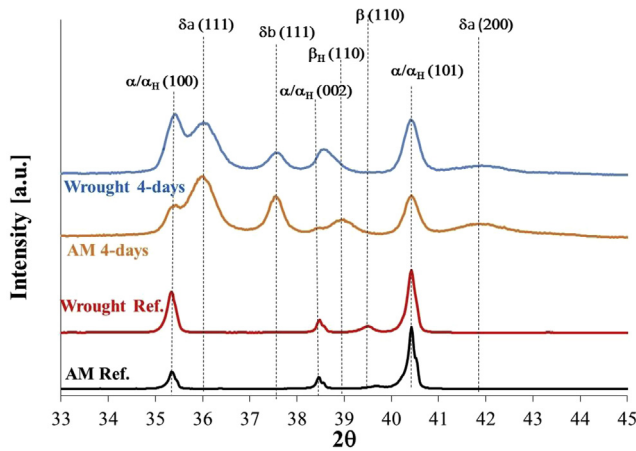


Fig. 4 – XRD patterns of non-hydrogenated and four-day hydrogenated EBM and wrought Ti–6Al–4V alloys.

space group Fm-3m (225). The presence of high-angle peaks, namely the (222) plane at just under $2\theta = 81$ deg, support the presence of such a smaller cubic phase. Fig. S6 shows a TOPAS Rietveld refinement (weighted profile R-factor, $R_{wp} = 13.02$) of a typical X-ray diffractogram of hydrogenated Ti–6Al–4V sample. All four phases claimed by us yield a strong fit.

The diffractograms of the hydrogenated samples did not change significantly with increasing hydrogenation time, indicating that the material surface reached steady state already after the first day of charging (i.e., hydride penetration is larger than the X-ray beam penetration). A similar behavior as a function of charging time (not shown here) was observed for the wrought alloy.

XRD patterns of EBM and wrought alloys in the non-hydrogenated and four-day hydrogenated conditions are shown in Fig. 4. Both non-hydrogenated alloys consist of the same phases, and so are the hydrogenated EBM and wrought alloys. The α/α_H , δ_a , and δ_b reflections were at similar angles in the wrought and EBM alloys. In contrast, the β/β_H reflections of

the wrought material were shifted to lower angles in comparison to the β/β_H reflections of the EBM material, indicating larger unit cells of the two phases in the wrought material. The original crystallographic orientations of the α -phases in both alloys did not change due to hydrogenation.

The lattice parameters and phase content (wt%) of both non-hydrogenated and hydrogenated alloys are listed in Table 3. The phase contents in each hydrogenated alloy are presented in terms of mean and standard deviation for all hydrogenation periods combined due to the similarity in peak positions during 1–4 day charging periods. For the same reason, the lattice parameters in the hydrogenated alloys are the minimum and maximum values that were obtained for all hydrogenation periods. It is evident that both non-hydrogenated alloys contained a similar amount of β -phase (6.13 and 6.87 wt% in the wrought and EBM alloys, respectively). This is higher than the value of 2.5 ± 1.4 wt% which was previously reported for the EBM material [62]. After hydrogenation, the $\beta+\beta_H$ content in both alloys is similar to the original β content, but the lattice parameters of the β_H -phase expanded by 2.07% and 1.84% in the wrought and EBM alloys, respectively. This expansion is expected due to high solubility of hydrogen in the β -phase. In contrast, the lattice parameters of the α/α_H -phases were similar to the lattice parameters of the α -phase in the non-hydrogenated alloys, due to the low solubility of hydrogen in the α -phase.

The $\alpha+\alpha_H$ content in both alloys decreased significantly compared to the α -phase content in the non-hydrogenated alloys, by 58% and 78% in the wrought and EBM alloys respectively. The δ_a -phase content in the wrought material was about 2/3 of its content in the EBM material, while the δ_b -phase content was similar in both hydrogenated alloys. This suggests that the tendency of α -phase to transform to δ_a hydride during hydrogenation is higher in the EBM material than in the wrought material.

In principal, a different hydrogen behavior in the EBM alloy compared to the wrought alloy may result from different microstructures, porosity, and residual stresses (or microstrains). The latter was evaluated based on XRD data analysis.

Table 3 – Lattice parameters and phase content in the non-hydrogenated wrought and EBM alloys as well as after hydrogenation ($n = 4$ for each hydrogenated alloy). The phase contents in the hydrogenated alloys are presented in terms of means and standard deviations for all hydrogenation periods. The lattice parameters in the hydrogenated alloys are the minimum and maximum values that were obtained for all hydrogenation periods.

	Wrought alloy			EBM alloy		
	a, b (Å)	c (Å)	Content (wt%)	a, b (Å)	c (Å)	Content (wt%)
Non-hydrogenated						
α	2.9266	4.6699	93.87	2.9246	4.6698	93.13
β	3.2208		6.13	3.1995		6.87
Hydrogenated						
α/α_H	2.9230	4.6692	39.3 ± 5.7	2.9202	4.6635	20.6 ± 5.0
	2.9258	4.6791		2.9255	4.6679	
β_H	3.2821		6.4 ± 0.5	3.2567		6.2 ± 0.5
	3.2921			3.2593		
δ_a	4.3053		44.8 ± 4.0	4.3075		60.2 ± 5.5
	4.3131			4.3116		
δ_b	4.1407		9.5 ± 5.3	4.1351		13.0 ± 1.2
	4.1530			4.1419		

The microstrains in the non-hydrogenated EBM and wrought alloys were $4 \pm 1 \times 10^{-4}$ and $3 \pm 1 \times 10^{-4}$, respectively, in the α -phase and zero in the β -phase. Therefore, different behavior of hydrogen in both alloys cannot be attributed to different residual stresses due to different processing routes. Pushilina et al. [86] showed that the microstrain in the α -phase decreased from $3.0 \pm 0.1 \times 10^{-3}$ to $1.3 \pm 0.1 \times 10^{-3}$ as the beam current was increased from 2.5 to 3.5 mA. In the present study, the beam current was 28 mA, hence the value reported above for the EBM alloy is reasonable. After two-day hydrogenation, the microstrains in the α/α_H -phase increased to $15 \pm 2 \times 10^{-4}$ and $24 \pm 1 \times 10^{-4}$ in the EBM and wrought alloys, respectively. After four-day hydrogenation, the measured values were $20 \pm 2 \times 10^{-4}$ and $23 \pm 1 \times 10^{-4}$, respectively. The microstrains in the β_H -phase also increased due to hydrogenation, to $51 \pm 3 \times 10^{-4}$ and $46 \pm 4 \times 10^{-4}$ in the EBM and wrought alloys, respectively. The microstrains in the δ_a -hydride were $63 \pm 2 \times 10^{-4}$ and $54 \pm 1 \times 10^{-4}$ in the EBM and wrought alloys,

respectively, after two-day hydrogenation; and $57 \pm 0.6 \times 10^{-4}$ and $63 \pm 2 \times 10^{-4}$, respectively, after four-day hydrogenation. The equivalent values for the δ_b -hydride were $36 \pm 1 \times 10^{-4}$ and $25 \pm 1 \times 10^{-4}$, respectively, after two-day hydrogenation; and $34 \pm 1 \times 10^{-4}$ and $18 \pm 2 \times 10^{-4}$, respectively, after four-day hydrogenation. Thus, it may be concluded that there does not appear to be any major microstrain difference between the EBM and wrought alloys, either before or after hydrogenation.

TEM microstructural characterization of four-day hydrogenated EBM alloy

TEM imaging, selected area electron diffraction (SAED) and local EDS analysis were used to associate crystallographic phases with microscopic appearance and chemical composition in the EBM alloy hydrogenated for four days. The TEM sample was extracted from the surface of a four-day hydrogenated sample (similar to the XRD analysis location). The $\alpha/$

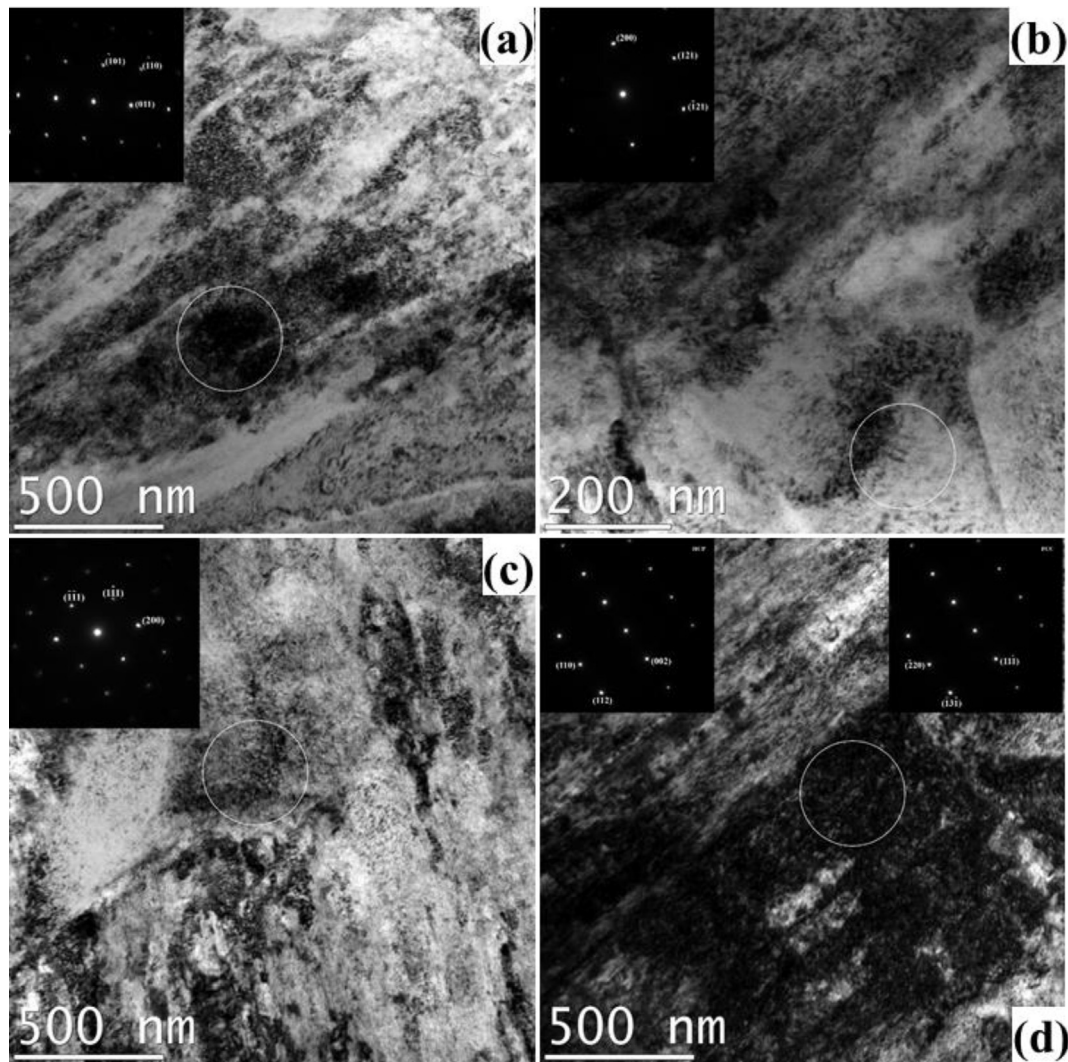


Fig. 5 – Bright-field TEM micrographs and corresponding SAED patterns acquired from a four-day hydrogenated EBM Ti–6Al–4V alloy. (a) α/α_H , (b) β_H , (c) δ_a -hydride, and (d) two possibilities – α/α_H (left inset) or δ_b -hydride (right inset).

α_{H} -phase was identified with hexagonal structure (Fig. 5a) and lattice parameters $a = 2.932 \text{ \AA}$, $c = 4.643 \text{ \AA}$. Its approximate chemical composition was 92.7 Ti, 4.7 Al, 2.6 V (wt%), i.e., the local vanadium concentration was lower than the nominal composition in the non-hydrogenated alloy. The β_{H} -phase was identified with a cubic structure (Fig. 5b) and a lattice parameter $a = 3.272 \text{ \AA}$. Its local chemical composition was 69.7 Ti, 0.8 Al, 25.5 V, and 3.9 Fe (wt%). The high vanadium concentration indicates V-to-Ti substitution when β is transformed to β_{H} .

The δ_{a} -hydride phase with a cubic structure having the Fm-3m space group (Fig. 5c) and a lattice parameter $a = 4.28 \pm 0.04 \text{ \AA}$ was identified. Its local chemical composition was 80.7 Ti, 1.8 Al, 15.9 V, and 1.7 Fe (wt%). The high content of vanadium in δ_{a} , which was reported before [87], may explain the smaller lattice parameter of this phase compared to δ -TiH₂ and δ -TiH_x hydrides. Vanadium is known to reduce the lattice parameter of MH₂ ($M = \text{Ti} + \text{V}$) while substituting Ti. On the two extremes, the lattice parameter a is reduced from 4.448 Å for TiH₂ (ICDD no. 00-025-0982) to 4.268 Å for VH₂ (ICDD no. 01-071-4967). The SAED of the phase shown in Fig. 5d may be attributed to either hcp α/α_{H} (left inset in Fig. 5d, $a = 2.9202 \text{ \AA}$, $c = 4.6635 \text{ \AA}$) or fcc δ_{b} -hydride (right inset in Fig. 5d, $a = 4.1476$).

The reason for this uncertainty is overlapping of the interplanar distances of the phases – $\alpha(110)$ with $\delta_{\text{b}}(220)$. The local chemical composition (EDS) – 93.7 Ti, 4.0 Al, 2.3 V – favors the identification of the phase in Fig. 5d as α/α_{H} . The inability to identify unambiguously the δ_{b} hydride phase by TEM does not undercut its identification by XRD, which better reflects the average phase composition adjacent to the sample surface.

ToF-SIMS analysis

Fig. 6 shows ToF-SIMS image mapping of the total hydrogen intensity and the titanium hydride intensity in wrought and EBM samples. The total hydrogen intensity is comprised of solute hydrogen, surface adsorbed hydrogen, noise, etc. The fact that hydrides were clearly evident in Fig. 6b,d and that the microstructure of the Ti alloys correspond well with that in Fig. 1e,f and Fig. 2e,h implies that the signal-to-noise ratio is sufficiently high for some meaningful analysis. From Fig. 6 it may be concluded that hydrides are aligned in parallel to interphase boundaries and that higher structural complexity exists in the EBM alloy compared to the wrought alloy. The dark areas in this figure may be related to the less

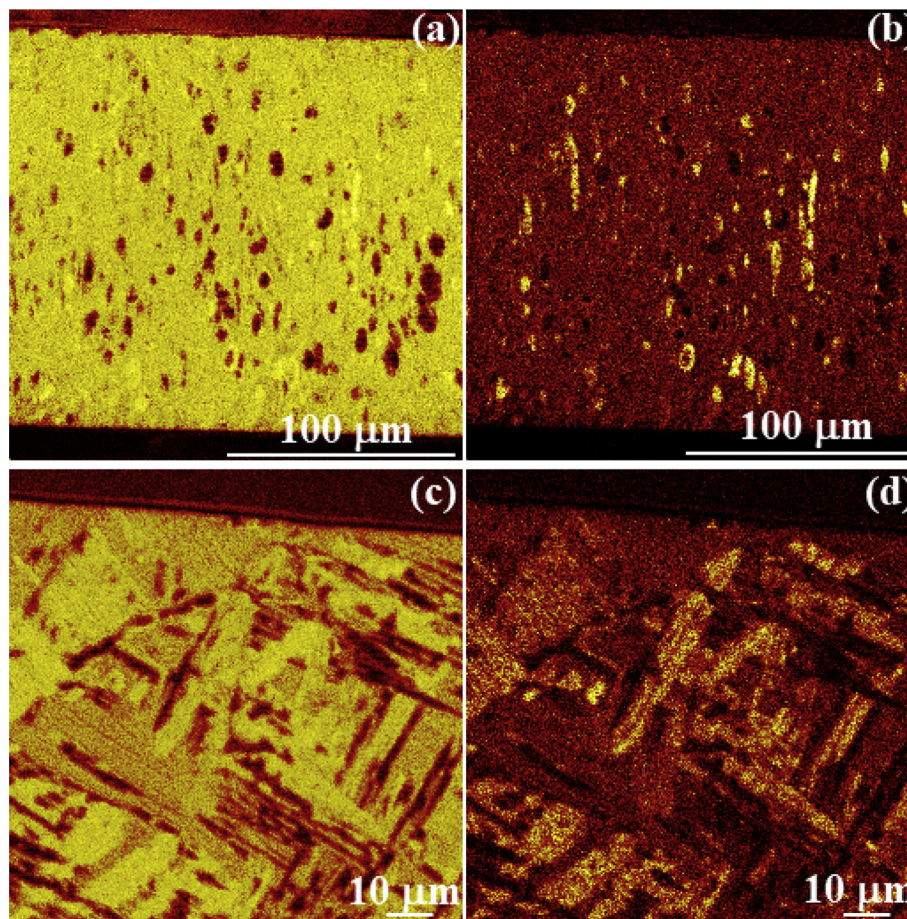


Fig. 6 – ToF-SIMS image mapping of the total hydrogen intensity (a,c) and the titanium hydride intensity (b,d) in wrought (a,b) and EBM (c,d) samples. (a,b) Reveal the whole cross-section, whereas (c,d) reveal the upper side of the cross-section. Brighter areas indicate higher signal (concentration) of hydrogen.

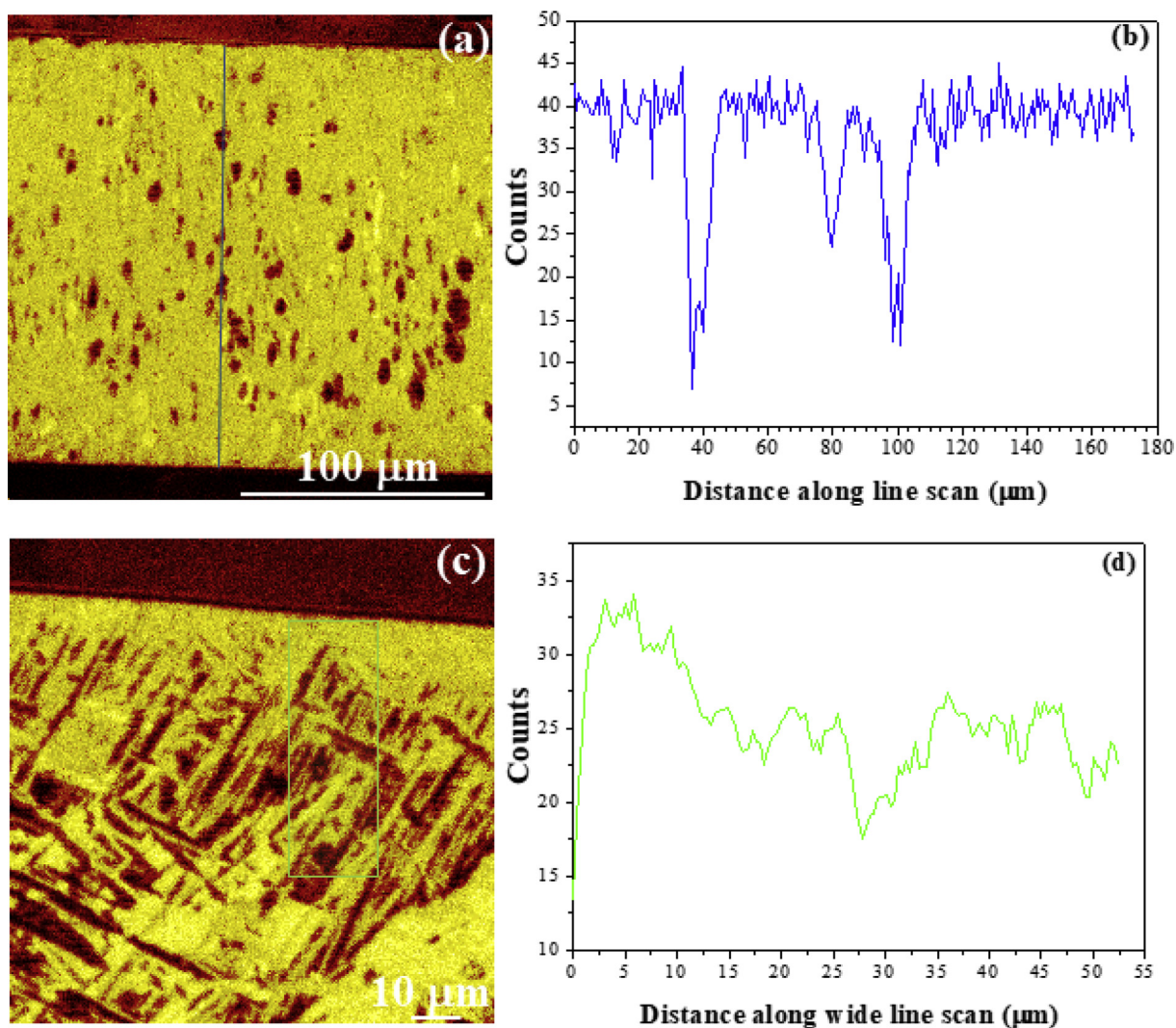


Fig. 7 – ToF-SIMS line scan profiling of the total hydrogen concentration. A narrow line scan in the wrought alloy (a) and the corresponding concentration profile (b). A broad line scan in the EBM alloy (c) and the corresponding concentration profile (d).

hydrogenated α -phase. In a small fraction of the hydrides, oxygen and carbon impurities were detected.

Fig. 7a draws a narrow (blue) line scan on Fig. 6a in order to construct the profile of the total hydrogen concentration across the thickness of the wrought sample. The profile itself is shown in Fig. 7b. A similar behavior was observed by SIMS in the case of the EBM alloy (not shown herein). It may be concluded that hydrogen absorption in the wrought alloy is not limited to the near-surface region, but instead hydrogen penetrates through the whole bulk sample. Comparing Fig. 7b with Fig. 7a it is also concluded that low local concentration of hydrogen may be related to the less hydrogenated α -phase. These large hydrogen intensity variations emanating from different phases required that any comparison between the samples was made using an average hydrogen content within the analysis area.

SEM revealed in the cross-section of hydrogenated EBM alloy a near-surface region with morphology different from the majority of the bulk sample (see Fig. 2h,j for one- and four-day charging, respectively). Such a distinguished layer was

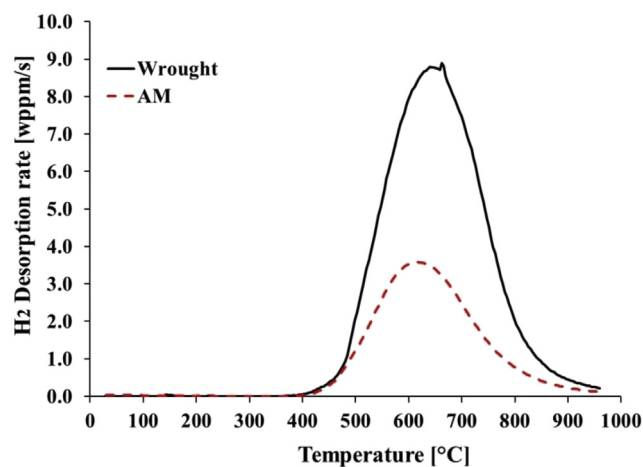


Fig. 8 – H₂-TPD spectra for wrought and EBM specimens precharged with hydrogen for four days. The spectra were measured at a heating rate of 15 °C/min.

not observed by light microscopy (Fig. 1). Hydride mapping by SIMS did not reveal it either. This cannot be related to high noise-to-signal because other microstructural features in the SIMS image can be seen. Nevertheless, mapping of total hydrogen by SIMS may reveal this layer (Fig. 7c). A broad line scan (marked by the green rectangle in Fig. 7c) yielded the total hydrogen profile shown in Fig. 7d. It is evident that the near-surface region with distinct morphology is richer in hydrogen compared to the bulk sample.

Fig. S7 shows the average normalized intensities H/Ti and TiH_x/Ti , as determined by SIMS. No significant difference in the hydrogen content (in its different forms) was detectable when comparing the wrought alloy to the EBM alloy. However, it should be borne in mind that SIMS provides only local chemical analysis, and only of one sample from each alloy in this study. Therefore, the similarity in the total hydrogen concentration might be misleading, and a bulk analysis of significantly larger sample volumes is preferable. This was achieved in this study by TPD (see Section TPD analysis below). Mass spectra (not shown herein) indicated that in both alloys the hydrides were of the same type, in accordance with the XRD results presented above.

TPD analysis

The thermal desorption spectra of H_2 from the wrought and EBM specimens hydrogenated for 4 days are presented in Fig. 8. It can be seen that for both alloys hydrogen desorption initiates at $\sim 400^\circ\text{C}$, with a single desorption peak at $\sim 620^\circ\text{C}$. The amount of desorbed hydrogen, obtained by integrating the H_2 -TPD spectra, is 5900 ± 1800 wtppm (4 samples) and 3500 ± 400 wtppm (3 samples) for the wrought and EBM specimens, respectively. The hydrogen contents desorbed from the wrought and AM Ti–6Al–4V alloys after two- and three-day charging are summarized in Table S1.

Discussion

In this work, we compared the hydrogen behavior in EBM and wrought Ti–6Al–4V alloys to determine the role of microstructure. Hydrogen was introduced into the alloys electrochemically via one-, two-, three-, and four-day charging. However, this article focuses mostly on the comparison between non-hydrogenated and four-day hydrogenated alloys.

It was shown that the hydrogenated EBM alloy was more prone to hydrogen cracking along interphase boundaries. Both non-hydrogenated alloys showed similar values of density (Section Chemical composition and density), microstrain, and β -phase content (Section XRD phase and microstrain analysis) and, therefore, the differences in hydrogen behavior in the two alloys cannot be attributed to these microstructural features. The higher susceptibility to hydrogen embrittlement of the EBM alloy can be attributed to the finer needle-like, smaller lattice constants and non-continuous β -phase particles in the EBM alloy. The path of microcracking observed by light microscopy and SEM, and hydride arrangement observed by SIMS mapping, support this conclusion.

The phase composition at the surface of both alloys reached steady state already after one day of charging, and

consisted of α/α_{H} (hcp) and β_{H} (bcc) solid solutions as well as two hydrides – δ_{a} (fcc) and δ_{b} (fcc), with lattice parameters that have not been reported before and are smaller than those of δ -TiH₂ and δ -TiH_x. Extension of the present work may thus result in new International Center for Diffraction Data (ICDD) files for these hydrides.

While the δ_{b} -content was similar in both alloys, the δ_{a} -phase content was higher in the EBM alloy. Furthermore, the unit cells of the β (non-hydrogenated) and β_{H} phases were larger in the wrought alloy than in the EBM alloy. The lattice parameters of the β_{H} phases were expanded due to hydrogenation and the high solubility of hydrogen in the β -phase. In contrast, the lattice parameters of the α/α_{H} phases were similar to the lattice parameters of the α -phase in the non-hydrogenated alloys due to the low solubility of hydrogen in the α -phase. The β_{H} content was similar to the original β -content of the non-hydrogenated alloys, suggesting that the two hydride phases transformed from the primary α -phase. Indeed, the $\alpha+\alpha_{\text{H}}$ content in both alloys decreased significantly compared to the α -content in the non-hydrogenated alloys. The δ_{a} -content in the wrought material was about 2/3 of its content in the EBM material, while the δ_{b} -content was similar in both hydrogenated alloys. This suggests that the tendency of the α -phase to transform to δ_{a} hydride during hydrogenation was higher in the EBM material than in the wrought material, and therefore the wrought material contained less hydrides at its surface. It should be noted that surface hydrides on titanium have been observed following different electrochemical processes, such as galvanic coupling of titanium to a less noble material [88], acid etching [89], or cathodic polarization [49,90]. The number of publications reporting hydride formation in the bulk alloy due to electrochemical charging is significantly lower (see, for example [70]).

The simultaneous presence of δ_{a} and δ_{b} hydride phases is attributed to the relatively small content of β -phase in the non-hydrogenated alloys, which resulted in relatively low diffusivity and solubility of hydrogen in these alloys and facilitated the preferable nucleation and growth of δ -hydrides at α/β interphases [82]. The lower diffusivity and solubility of hydrogen in the EBM alloy compared to the wrought alloy, due to their different microstructures, favored the $\alpha/\alpha_{\text{H}} \rightarrow \delta_{\text{a}}$ phase transformation in vicinity to the surface of the EBM alloy. This could both inhibit hydrogen entry from the environment and serve as a source of hydrogen into the bulk alloy when sufficient energy is employed to decompose the hydride. The microstrains in the α/α_{H} and β_{H} phases in the hydrogenated alloys were higher than those in the α and β phases in the non-hydrogenated alloys; the largest microstrains evolved in the β_{H} and δ_{a} phases.

For both alloys precharged for four days, the hydrogen content values (~ 0.35 – 0.6 wt%) were lower compared to the full hydrogen capacity reported for wrought Ti–6Al–4V alloy in powder form [14]. This suggests that in the current study the hydrogenation conditions were milder, surface layers acted as a barrier for either hydrogen absorption or hydrogen desorption, or some hydrogen remained strongly trapped in the alloys even when reaching the maximal measurement temperature (950°C).

The higher hydrogen content desorbed from the wrought alloy compared to the EBM material is in opposite trend to the hydride contents in both alloys based on XRD (see Table 3). A possible explanation could be that not all hydride decomposed to desorb hydrogen from the sample when reaching the maximal measurement temperature of 950 °C in the TPD tests. However, a complementary measurement of the hydrogen content in the samples after TPD tests, by inert gas fusion technique, showed that no residual hydrogen was left in the samples (i.e., all absorbed hydrogen was desorbed during heating to 950 °C in the TPD measurements). The lower hydrogen uptake in the bulk EBM alloy compared to the wrought alloy after four-day hydrogenation could thus be explained by the formation of a barrier hydride surface layer on the EBM alloy [52]. However, such a hydride layer was not detected by SIMS. Another possible explanation to the higher solubility of hydrogen in the wrought alloy is its lower solute oxygen content (see Section Chemical composition and density and Table 1). It has been reported that interstitial oxygen decreases the hydrogen solubility in titanium at a fixed pressure [91–93], possibly due to the blocking effect [92] and the decreases in partial molar enthalpy and excess entropy of hydrogen [91,93]. High interstitial oxygen content could thus favor precipitation of the brittle hydride phase. If so, one of the approaches to decrease the susceptibility of AM Ti–6Al–4V alloy to hydrogen embrittlement and hydrogen-induced cracking may be to use a Grade 23 powder (ELI, maximum 0.13 wt% oxygen according to ASTM F3001 standard) instead of Grade 5 powder (maximum 0.20 wt% oxygen according to ASTM F2924 standard). Yet, it should be noted that the concentration of oxygen in Ref. [91–93] was 5–42.9 at%, significantly higher than either in the present study or in the ASTM standards referred to above.

The significantly higher value of standard deviation in the hydrogen content desorbed from the wrought alloy compared to the EBM counterpart (pre-charged for four days) may be attributed to non-uniform distribution of the α -phase and the lamellar structure in the bulk wrought alloy (see Section Microstructure and local chemical composition). On the other hand, it cannot be related to variance in the experimental conditions during electrochemical hydrogenation and/or in the TPD system since the repeatability of results was high in the case of the EBM alloy.

Both the wrought and the EBM alloys were embrittled by hydrogen; however, the microstructure of the EBM alloy with more α/β interphases promoted the α/α_H -to- δ_a phase transformation and made the EBM alloy more prone to hydrogen-induced cracking along interphase boundaries compared to the wrought alloy. Hence, a post-treatment that increases the size of the β particles may help improving the resistance of EBM Ti–6Al–4V to hydrogen-induced damage. Hydrogenation resulted in formation of microvoids, either adjacent to the surface or along interphase interfaces, their coalescence, and emanation of microcracks around them. Porosity in electron beam welded commercially pure (CP) titanium and electrochemically charged Ti–6Al–4V has been attributed to hydrogen diffusion-controlled bubble growth [94]. However, the mechanism of hydrogen-related microvoid formation in the current study seems to be different. One of the proposed

hydrogen embrittlement mechanisms is the high-pressure bubble formation mechanism, according to which bubbles filled with molecular hydrogen can develop in iron and other metals with endothermic heat of hydrogen solution under conditions of high hydrogen fugacity [95–97]. However, titanium has exothermic heat of solution for hydrogen. Thus, the mechanism of formation of hydrogen-related bubbles in the wrought and EBM Ti–6Al–4V alloys is puzzling; its understanding requires further research.

Conclusions

The effects of the microstructures of electron beam melting (EBM) additive manufacturing (AM) and wrought Ti–6Al–4V alloys on their interaction with hydrogen charged electrochemically were studied. The following conclusions were drawn:

- 1 A lower lattice constant of the β -phase, a larger amount of α/β interphases, and discontinuous arrangement of β -phase particles along the short-transverse direction in the EBM alloy compared to the wrought alloy, enhanced hydride and microvoids formation, promoted hydrogen cracking along interphase boundaries, and thus increased the EBM alloy susceptibility to hydrogen embrittlement.
- 2 The surface of the hydrogenated alloys reached steady state after one day of charging and consisted of α/α_H (hcp) and β_H (bcc) solid solutions as well as δ_a (fcc) and δ_b (fcc) hydrides that have not been reported before, even not by the ICDD. These hydrides transformed from the original α phase.
- 3 Hydrogen desorption was lower from the EBM alloy than from the wrought alloy. This could be due to the higher solute oxygen content, non-continuous arrangement of β -phase in the short-transverse direction, and a smaller lattice constant of the β -phase in the EBM alloy. The effect of a possible formation of a barrier hydride surface layer on the EBM alloy cannot be ruled out either.

The use of a post-treatment that would increase the size of the β particles is suggested to improve the resistance of EBM Ti–6Al–4V to hydrogen-induced damage.

Declaration of competing interest

The authors declare that they have no known competing financial interests or personal relationships that could have appeared to influence the work reported in this paper.

Acknowledgements

The authors thank Mr. Michael Chonin from Rotem Industries Ltd. for AM EBM of Ti–6Al–4V, Dr. Eswar Komarala and Mr. Eliran Hamo from TAU for XRD measurements, Dr. Alexander Gladkikh from the Wolfson Applied Materials Research Center at TAU for ToF-SIMS analysis, Mrs. Natalie Kostirya from

NRCN for TPD measurements, Ms. Einat Strumza from BGU for chemical analysis, Mr. Nadav Guy from NRCN for gas analysis, Mr. David Noiman from NRCN for density measurements, Dr. Elad N. Caspi and Dr. Asaf Pesach from NRCN for XRD Round Robin of the β -content in the non-hydrogenated alloy, Prof. Yuval Goren from BGU for XRF analysis of the black residues, Mr. Atzmon Vakahi from the Hebrew University in Jerusalem for FIB sample preparation, Mr. Mario Levinshtein, Mr. Igor Hohotkin, Mr. David Eliyahu and Mr. David Svetlizky from TAU, and Mr. David Hai David from NRCN, for general technical assistance.

Appendix A. Supplementary data

Supplementary data to this article can be found online at <https://doi.org/10.1016/j.ijhydene.2020.06.277>.

REFERENCES

- [1] Veiga C, Davim JP, Loureiro AJR. Properties and applications of titanium alloys: a brief review. *Rev Adv Mater Sci* 2012;32:133–48.
- [2] Eliaz N. Corrosion of metallic biomaterials: a review. *Materials* 2019;12:407.
- [3] Eliaz N, Eliezer D, Olson DL. Hydrogen-assisted processing of materials. *Mater Sci Eng A* 2000;289:41–53.
- [4] Eliezer D, Eliaz N, Senkov ON, Froes FH. Positive effects of hydrogen in metals. *Mater Sci Eng A* 2000;280:220–4.
- [5] Paramore JD, Fang ZZ, Dunstan M, Sun P, Butler BG. Hydrogen-enabled microstructure and fatigue strength engineering of titanium alloys. *Sci Rep* 2017;7:41444.
- [6] Ding R, Guo ZX, Wilson A. Microstructural evolution of a Ti–6Al–4V alloy during thermomechanical processing. *Mater Sci Eng A* 2002;327:233–45.
- [7] Kohn DH, Ducheyne P. Microstructural refinement of β -sintered and Ti-6Al-4V porous-coated by temporary alloying with hydrogen. *J Mater Sci* 1991;26:534–44.
- [8] Hong S-B, Eliaz N, Sachs EM, Allen SM, Latanision RM. Corrosion behavior of advanced Ti-based alloys made by three-dimensional printing (3DP™) for biomedical applications. *Corrosion Sci* 2001;43:1781–91.
- [9] Madina V, Azkarate I. Compatibility of materials with hydrogen. Particular case: hydrogen embrittlement of titanium alloys. *Int J Hydrogen Energy* 2009;34:5976–80.
- [10] Eliaz N, Gileadi E. *Physical Electrochemistry: Fundamentals, Techniques, and Applications*. 2nd ed. Weinheim, Germany: Wiley-VCH; 2019. Ch. 17.
- [11] Fukai Y. *The Metal-Hydrogen System*. New York, USA: Springer-Verlag; 1993. p. 22.
- [12] Christ H-J, Decker M, Zeitler S. Hydrogen diffusion coefficients in the titanium alloys IMI 834, Ti 10-2-3, Ti 21 S, and alloy C. *Metall Mater Trans A* 2000;31:1507–17.
- [13] Luo L, Su Y, Guo J, Fu H. Formation of titanium hydride in Ti–6Al–4V. *J Alloys Compd* 2006;425:140–4.
- [14] Blackburn JL, Parilla PA, Gennett T, Hurst KE, Dillon AC, Heben MJ. Measurement of the reversible hydrogen storage capacity of milligram Ti–6Al–4V alloy samples with temperature programmed desorption and volumetric techniques. *J Alloys Compd* 2008;454:483–90.
- [15] Liu HJ, Zhou L, Liu P, Liu QW. Microstructural evolution and hydride precipitation mechanism in hydrogenated Ti–6Al–4V alloy. *Int J Hydrogen Energy* 2009;34:9596–602.
- [16] Zhu T, Li M. Effect of 0.770 wt%H addition on the microstructure of Ti–6Al–4V alloy and mechanism of δ hydride formation. *J Alloys Compd* 2009;481:480–5.
- [17] Pushilina N, Syrtanov M, Kashkarov E, Murashkina T, Kudiiarov V, Laptev R, Lider A, Koptyug A. Influence of manufacturing parameters on microstructure and hydrogen sorption behavior of electron beam melted titanium Ti-6Al-4V alloy. *Materials* 2018;11:763.
- [18] Pushilina N, Panin A, Syrtanov M, Kashkarov E, Kudiiarov V, Perevalova O, Laptev R, Lider A, Koptyug A. Hydrogen-induced phase transformation and microstructure evolution for Ti-6Al-4V parts produced by electron beam melting. *Metals* 2018;8:301.
- [19] Hirohata Y, Aihara Y, Hino T, Miki N, Nakagawa S. Evaluation of hydrogen sorption and desorption for Ti-6Al-4V alloy as a vacuum vessel material. In: Varandas C, Serra F, editors. *Proc. 19th symp. Fusion technology 1996*, vol. 1. New York, NY, USA: Elsevier; 1997. p. 363–6.
- [20] Okamoto H. H-Ti (hydrogen-titanium). *J Phase Equilib Diffus* 2011;32:174–5.
- [21] Takasald A, Furuya Y, Ojima K, Taneda Y. Hydride dissociation and hydrogen evolution behavior of electrochemically charged pure titanium. *J Alloys Compd* 1995;224:269–73.
- [22] Wu T-I, Wu J-K. Effects of electrolytic hydrogenating parameters on structure and composition of surface hydrides of CP-Ti and Ti–6Al–4V alloy. *Mater Chem Phys* 2002;74:5–12.
- [23] Tal-Gutelmacher E, Eliezer D. High fugacity hydrogen effects at room temperature in titanium based alloys. *J Alloys Compd* 2005;404–406:613–6.
- [24] Sun P, Fang ZZ, Koopman M, Paramore J, Ravi Chandran KS, Ren Y, Lu J. An experimental study of the (Ti–6Al–4V)–xH phase diagram using in situ synchrotron XRD and TGA/DSC techniques. *Acta Mater* 2015;84:29–41.
- [25] Ma M, Liang L, Wang L, Wang Y, Cheng Y, Tang B, Xiang W, Tan X. Phase transformations of titanium hydride in thermal desorption process with different heating rates. *Int J Hydrogen Energy* 2015;40:8926–34.
- [26] Silverstein R, Eliezer D. Hydrogen trapping in 3D-printed (additive manufactured) Ti-6Al-4V. *Mater Char* 2018;144:297–304.
- [27] Hong S-B, Eliaz N, Leisk GG, Sachs EM, Latanision RM, Allen SM. A new Ti-5Ag alloy for customized prostheses by three-dimensional printing (3DP™). *J Dent Res* 2001;80:860–3.
- [28] Seyda V, Herzog D, Emmelmann C. Relationship between powder characteristics and part properties in laser beam melting of Ti–6Al–4V, and implications on quality. *J Laser Appl* 2017;29:22311–8.
- [29] Zhai Y, Galarraga H, Lados DA. Microstructure, static properties, and fatigue crack growth mechanisms in Ti-6Al-4V fabricated by additive manufacturing: LENS and EBM. *Eng Fail Anal* 2016;69:3–14.
- [30] Kok Y, Tan XP, Wang P, Nai MLS, Loh NH, Liu E, Tor SB. Anisotropy and heterogeneity of microstructure and mechanical properties in metal additive manufacturing: a critical review. *Mater Des* 2018;139:565–86.
- [31] Herzog D, Seyda V, Wycisk E, Emmelmann C. Additive manufacturing of metals. *Acta Mater* 2016;117:371–92.
- [32] Rafi HK, Karthik NV, Gong H, Starr TL, Stucker BE. Microstructures and mechanical properties of Ti6Al4V parts fabricated by selective laser melting and electron beam melting. *J Mater Eng Perform* 2013;22:3872–83.
- [33] Tiferet E, Rivin O, Ganor M, Etedgui H, Ozeri O, Caspi EN, Yeheskel O. Structural investigation of selective laser melting and electron beam melting of Ti-6Al-4V using neutron diffraction. *Addit Manuf* 2016;10:43–6.

- [34] Murr LE, Quinones SA, Gaytan SM, Lopez MI, Rodela A, Martinez EY, Hernandez DH, Martinez E, Medina F, Wicker RB. Microstructure and mechanical behavior of Ti–6Al–4V produced by rapid-layer manufacturing, for biomedical applications. *J Mech Behav Biomed Mater* 2009;2:20–32.
- [35] Zhao X, Li S, Zhang M, Liu Y, Sercombe TB, Wang S, Hao Y, Yang R, Murr LE. Comparison of the microstructures and mechanical properties of Ti–6Al–4V fabricated by selective laser melting and electron beam melting. *Mater Des* 2016;95:21–31.
- [36] Murr LE, Gaytan SM, Ramirez DA, Martinez E, Hernandez J, Amato KN, Shindo PW, Medina FR, Wicker RB. Metal fabrication by additive manufacturing using laser and electron beam melting technologies. *J Mater Sci Technol* 2012;28:1–14.
- [37] Al-Bermani SS, Blackmore ML, Zhang W, Todd I. The origin of microstructural diversity, texture, and mechanical properties in electron beam melted Ti-6Al-4V. *Metall Mater Trans A* 2010;41:3422–34.
- [38] Kudiiarov VN, Syrtanov MS, Bordulev YuS, Babikhina MN, Lider AM, Gubin VE, Murashkina TL. The hydrogen sorption and desorption behavior in spherical powder of pure titanium used for additive manufacturing. *Int J Hydrogen Energy* 2017;42:15283–9.
- [39] Murr LE. Metallurgy of additive manufacturing: examples from electron beam melting. *Addit Manuf* 2015;5:40–53.
- [40] Stepanova E, Pushilina N, Syrtanov M, Laptev R, Kashkarov E. Hydrogen effect on Ti–6.5Al–3.5Mo–1.5Zr–0.3Si parts produced by electron beam melting. *Int J Hydrogen Energy* 2019;44:29380–8.
- [41] Laptev R, Kudiiarov V, Pushilina N. Hydrogen influence on defect structure and mechanical properties of EBM Ti-6Al-4V. *Mater Today Proc* 2019;19:2084.
- [42] Gaddam R, Åkerfeldt P, Pederson R, Antti M-L. Influence of hydrogen environment on the mechanical properties of cast and electron beam melted Ti-6Al-4V. In: Zhou L, editor. *Ti–2011: proc. 12th world conf. on titanium*, vol. 3. Beijing, China: Social Sciences Academic Press; 2012. p. 1885–8.
- [43] Iyer RN, Pickering HW. Mechanism and kinetics of electrochemical hydrogen entry and degradation of metallic systems. *Annu Rep Mater Sci* 1990;20:299–338.
- [44] Verbeke K. Analysing hydrogen in metals: bulk thermal desorption (TDS) methods. In: Gangloff RP, Somerday BP, editors. *Gaseous Hydrogen Embrittlement of Materials in Energy Technologies*, Vol. 2. Cambridge, UK: Woodhead Publishing Limited; 2012. p. 27–55. Ch. 2.
- [45] Singh RN, Kishore R, Mukherjee S, Roychowdhury S, Srivastava D, Sinha TK, Dem PK, Bamerjee S, Kameswaran R, Sheelvantra SS, Gopalan B. Hydrogen charging, hydrogen content analysis and metallographic examination of hydride in zirconium alloys. Report no. BARC/2003/E/034. Mumbai, India: Bhabha Atomic Research Centre; 2003.
- [46] Lee JA. Hydrogen embrittlement. Report no. NASA/TM-2016–218602. Alabama: NASA Marshall Space Flight Center Huntsville; April 2016.
- [47] Oriani RA. The physical and metallurgical aspects of hydrogen in metals. Plenary session papers, TR-104188-V1. In: *Proc. 4th Int. Conf. on Cold Fusion*, vol. 1. Palo Alto, California: Electric Power Research Institute; 1994.
- [48] Wallaert E, Depover T, Arafin M, Verbeke K. Thermal desorption spectroscopy of NbC and NbN precipitates. *Metall Mater Trans A* 2014;45:2412–20.
- [49] Briant CL, Wang ZF, Chollockoop N. Hydrogen embrittlement of commercial purity titanium. *Corrosion Sci* 2002;44:1875–88.
- [50] Hirth JP. Effects of hydrogen on the properties of iron and steel. *Metall Trans A* 1980;11:861–90.
- [51] Eliaz N, Eliezer D, Abramov E, Zander D, Köster U. Hydrogen evolution from Zr-based amorphous and quasicrystalline alloys. *J Alloys Compd* 2000;305:272–81.
- [52] Hruška P, Čížek J, Knapp J, Lukáč F, Melikhova O, Mašková S, Havela L, Drahoukoupil J. Characterization of defects in titanium created by hydrogen charging. *Int J Hydrogen Energy* 2017;42:22557–63.
- [53] Kirchheim R, McLellan RB. Electrochemical methods for measuring diffusivities of hydrogen in palladium and palladium alloys. *J Electrochem Soc* 1980;127:2419–25.
- [54] Lobo L, Fernández B, Pereiro R. Depth profile analysis with glow discharge spectrometry. *J Anal At Spectrom* 2017;32:920–30.
- [55] Winchester MR, Payling R. Radio-frequency glow discharge spectrometry: a critical review. *Spectrochim Acta Part B* 2004;59:607–66.
- [56] Hatano Y, Shi J, Yoshida N, Futagami N, Oya Y, Nakamura H. Measurement of deuterium and helium by glow-discharge optical emission spectroscopy for plasma–surface interaction studies. *Fusion Eng Des* 2012;87:1091–4.
- [57] Dubent S, Mazard A. Characterization and corrosion behaviour of grade 2 titanium used in electrolyzers for hydrogen production. *Int J Hydrogen Energy* 2019;44:15622–33.
- [58] Spierings AB, Schneider M, Eggenberger R. Comparison of density measurement techniques for additive manufactured metallic parts. *Rapid Prototyp J* 2011;17:380–6.
- [59] Wits WW, Carmignato S, Zanini F, Vaneker THJ. Porosity testing methods for the quality assessment of selective laser melted parts. *CIRP Ann Manuf Technol* 2016;65:201–4.
- [60] Svetlizky D, Zheng B, Buta T, Zhou Y, Golan O, Breiman U, Haj-Ali R, Schoenung JM, Lavernia EJ, Eliaz N. Directed energy deposition of Al 5xxx alloy using laser engineered net shaping (LENS®). *Mater Des* 2020;192:108763.
- [61] Gong H, Rafi K, Gu H, Starr T, Stucker B. Analysis of defect generation in Ti–6Al–4V parts made using powder bed fusion additive manufacturing processes. *Addit Manuf* 2014;1:87–98.
- [62] Tiferet E, Ganor M, Zolotaryov D, Garkun A, Hadjadj A, Chonin M, Ganor Y, Noiman D, Halevy I, Tevet O, Yeheskel O. Mapping the tray of electron beam melting of Ti-6Al-4V: properties and microstructure. *Materials* 2019;12:1470.
- [63] Sol T, Hayun S, Noiman D, Tiferet E, Yeheskel O, Tevet O. Nondestructive ultrasonic evaluation of additively manufactured AlSi10Mg samples. *Addit Manuf* 2018;22:700–7.
- [64] ASTM E407–15. Standard practice for microetching metals and alloys. West Conshohocken, PA, USA: ASTM International; 2015.
- [65] Rodríguez-Carvajal J. Fullprof, program for Rietveld Refinement. Saclay, France: Laboratoire Léon Brillouin (CEA-CNRS); 1997.
- [66] Lisowski W, van den Berg AHJ, Leonard D, Mathieu HJ. Characterization of titanium hydride films covered by nanoscale evaporated Au layers: ToF-SIMS, XPS and AES depth profile analysis. *Surf Interface Anal* 2000;29:292–7.
- [67] Kossoy E, Khoptiar Y, Cytermann C, Shemesh G, Katz H, Sheinkopf H, Cohen I, Eliaz N. The use of SIMS in quality control and failure analysis of electrodeposited items inspected for hydrogen effects. *Corrosion Sci* 2008;50:1481–91.
- [68] Hamada S, Ohnishi K, Nishikawa H, Oda Y, Noguchi H. SIMS analysis of low content hydrogen in commercially pure titanium. *J Mater Sci* 2009;44:5692–6.
- [69] Mine N, Portier S, Martin M. Imaging and hydrogen analysis by SIMS in zirconium alloy cladding: a dual ion beam approach. *Surf Interface Anal* 2014;45:249–52.

- [70] Liu Y, Ren ZH, Liu J, Schaller RF, Asselin E. Electrochemical investigation and identification of titanium hydrides formed in mixed chloride sulfuric acid solution. *J Electrochem Soc* 2019;166:C3096–105.
- [71] Zhu Z, Shutthanandan V, Engelhard M. An investigation of hydrogen depth profiling using ToF-SIMS. *Surf Interface Anal* 2012;44:232–7.
- [72] Danon A, Avraham I, Koresh JE. Temperature programmed desorption-mass spectrometer with supersonic molecular beam inlet system. *Rev Sci Instrum* 1997;68:4359–63.
- [73] Zeppelin FV, Haluška M, Hirscher M. Thermal desorption spectroscopy as a quantitative tool to determine the hydrogen content in solids. *Thermochim Acta* 2003;404:251–8.
- [74] Ifergane S, Ben David R, Sabatani E, Carmeli B, Beeri O, Eliaz N. Hydrogen diffusivity and trapping in Custom 465® stainless steel. *J Electrochem Soc* 2018;165:C107–15.
- [75] Matijasevic B, Fiechter S, Zizak I, Görke O, Wanderka N, Schubert-Bischoff P, Banhart J. Decomposition behavior of as-received and oxidized TiH₂ powder. In: Danninger H, Rätz R, editors. *Proc. Euro PM2004 – powder metallurgy world congress & exhibition, vol. 4. Shrewsbury: European Powder Metallurgy Association; 2004. p. 149–55.*
- [76] Ben David R, Finkelstein Y, Nativ-Roth E, Danon A, Cohen D, Rabkin E. The role of surface coarsening and sintering during thermal decomposition of titanium hydride. *Int J Hydrogen Energy* 2019;44:6045–54.
- [77] ASTM F2924–14. Standard specification for additive manufacturing titanium-6 aluminium-4 vanadium with powder bed fusion. West Conshohocken, PA, USA: ASTM International; 2014.
- [78] ASTM F136–13. Standard specification for wrought titanium-6aluminium-4vanadium ELI (extra low interstitial) alloy for surgical implant applications (UNS R56401). West Conshohocken, PA, USA: ASTM International; 2013.
- [79] Vrancken B, Thijs L, Kruth J-P, Humbeeck JV. Heat treatment of Ti6Al4V produced by selective laser melting: microstructure and mechanical properties. *J Alloys Compd* 2012;541(2012):177–85.
- [80] Pitt F, Ramulu M. Influence of grain size and microstructure on oxidation rates in titanium alloy Ti-6Al-4V under superplastic forming conditions. *JMEPEG* 2004;13:727–34.
- [81] Neikter M, Åkerfeldt P, Pederson R, Antti ML. Microstructure characterisation of Ti-6Al-4V from different additive manufacturing processes. *IOP Conf Ser Mater Sci Eng* 2017;258:012007.
- [82] Kim J, Tasan CC. Microstructural and micro-mechanical characterization during hydrogen charging: an in situ scanning electron microscopy study. *Int J Hydrogen Energy* 2019;44:6333–43.
- [83] Ding YS, Tsay LW, Chen C. The effects of hydrogen on fatigue crack growth behaviour of Ti-6Al-4V and Ti-4.5Al-3V-2Mo-2Fe alloys. *Corrosion Sci* 2009;51:1413–9.
- [84] Numakura H, Koiwa M, Asano H, Izumi F. Neutron diffraction study of the metastable γ titanium deuteride. *Acta Metall* 1988;36:2267–73.
- [85] Syrtanov M, Garanin G, Kashkarov E, Pushilina N, Kudiiarov V, Murashkina T. Laboratory X-ray diffraction complex for in situ investigations of structural phase evolution of materials under gaseous atmosphere. *Metals* 2020;10:447.
- [86] Pushilina NS, Klimenov VA, Cherepanov RO, Kashkarov EB, Fedorov VV, Syrtanov MS, Lider AM, Laptev RS. Beam current effect on microstructure and properties of electron-beam-melted Ti-6Al-4V alloy. *J Mater Eng Perform* 2019;28:6165–73.
- [87] Chang Y, Breen AJ, Tarzimaghadam Z, Kürnsteiner P, Gardner H, Ackerman A, Radecka A, Bagot PAJ, Lu W, Li T, Jagle EA, Herbig M, Stephenson LT, Moody MP, Rugg D, Dye D, Ponge D, Raabe D, Gault B. Characterizing solute hydrogen and hydrides in pure and alloyed titanium at the atomic scale. *Acta Mater* 2018;150:273–80.
- [88] Charlot LA, Westerman RE. Low-temperature hydriding of Zircaloy-2 and titanium in aqueous solutions. *Electr Technol* 1968;6:132–7.
- [89] Szmukler-Moncler S, Bischof M, Nedir R, Ermrich M. Titanium hydride and hydrogen concentration in acid-etched commercially pure titanium and titanium alloy implants: a comparative analysis of five implant systems. *Clin Oral Impl Res* 2010;21:944–50.
- [90] Videm K, Lamolle S, Monjo M, Ellingsen JE, Lyngstadaas SP, Haugen HJ. Hydride formation on titanium surfaces by cathodic polarization. *Appl Surf Sci* 2008;255:3011–5.
- [91] Yamanaka S, Fujita Y, Uno M, Katsura M. Influence of interstitial oxygen on hydrogen solubility in metals. *J Alloys Compd* 1999;293–295:42–51.
- [92] Yamanaka S, Tanaka T, Tsuboi S, Miyake M. Effect of oxygen on solubility of hydrogen isotopes in titanium. *Fusion Eng Des* 1989;10:303–8.
- [93] Yamanaka S, Ogawa H, Miyake M. Effect of interstitial oxygen on hydrogen solubility in titanium, zirconium and hafnium. *J Less Common Met* 1991;172–174:85–94.
- [94] Huang JL, Warnken N, Gebelin J-C, Strangwood M, Reed RC. On the mechanism of porosity formation during welding of titanium alloys. *Acta Mater* 2012;60:3215–25.
- [95] Eliaz N, Moshe E, Eliezer S, Eliezer D. Hydrogen effects on the spall strength and fracture characteristics of amorphous Fe-Si-B alloy at very high strain rates. *Metall Mater Trans A* 2000;31:1085–93.
- [96] Eliaz N, Eliezer D. Hydrogen effects on an amorphous Fe-Si-B alloy. *Metall Mater Trans A* 2000;31:2517–26.
- [97] Eliaz N, Banks-Sills L, Ashkenazi D, Eliasi R. Modeling failure of metallic glasses due to hydrogen embrittlement in the absence of external loads. *Acta Mater* 2004;52:93–105.